A geological explanation for intraplate earthquake clustering complexity: the zeolite-bearing fault/fracture networks in the Adamello Massif (Southern Italian Alps)

E.D. Dempsey[1], R.E. Holdsworth[1], J. Imber[1], A. Bistacchi[2] and G. Di Toro[3,4]

1 = Dept of Earth Sciences, Durham University, Durham, UK

2 = Dipartimento di Scienze Geologiche e Geotecnologie, Università degli Studi di Milano Bicocca, Milano, Italy

3 = Dipartimento di Geoscienze, Università degli Studi di Padova,Padova, Italy

4 = Istituto Nazionale di Geofisica e Vulcanologia, Roma, Italy.

Corresponding Author:

E.D. DEMPSEY

Dept of Earth Sciences,

Science Block,

Durham University,

Durham,

DH1 3LE,

UK

Telephone: +44 (0) 191 3342356

Email: e.d.dempsey@durham.ac.uk

Abstract: Interconnected networks of faults and veins filled with hydrothermal minerals such as zeolite are widespread in many orogenic terrains. These fractures commonly form at relatively low temperatures (e.g. < 200°C) late in the tectonic history and represent significant phases of fluid flow and mineralisation during exhumation. Zeolite-bearing fractures spatially associated with the Gole Larghe Fault Zone in the Southern Italian Alps are preserved along an interconnected network of variably orientated pre-existing structures. They show evidence of repeated episodes of hydraulic tensile fracturing and small magnitude (total offsets <5m) shear displacements. We use geological observations and Coulomb stress modelling to propose that repeated seismogenic rupturing of larger offset faults led to local stress transfer and reactivation of widely distributed smaller pre-existing structures in the wall rocks. The differing orientations of the pre-existing features within what is assumed to have been a single regional stress field led to the simultaneous development of reverse, strike-slip and extensional faults. The kinematic diversity and cyclic nature of the hydraulically-assisted deformation suggest that the mineralised fracture systems represent a geological manifestation of intraplate micro-earthquake clusters associated with fluid migration episodes in the upper crust. Our observations highlight the role of crustal fluids and structural reactivation during earthquakes.

1. Introduction

It is well-known that some lower magnitude earthquake clusters are spatially and temporally associated with larger mainshock events along faults: these are referred to as *fore-* and *after-shock sequences* (e.g. Scholz, 2002 and references therein). In other instances multiple lower magnitude seismic events may be closely spaced in time and space, but no main shock is observed: these are known as *swarms* (Sykes 1970; Mogi, 1963). The latter are often – but by no means always – associated with volcanic or geothermal activity, whilst some may be artificially induced by fluid injection (e.g. see Fischer *et al.* 2013 and references therein).

The origins of the frequently observed kinematic and spatial complexity associated with low magnitude earthquakes – as illustrated, respectively, by their complex focal mechanism solutions and diffuse, cloud-like distributions (e.g. Shearer *et al*. 2003, Godano *et al.* 2013, Kassaras *et al.* 2014) – are matters of speculation and debate. In general, clustering activity seems to be strongly associated with fluid ingression: the stress perturbation induced by each event results in stress and fluid redistribution and, as a consequence, in the complex spatial evolution of the sequence (Kisslinger, 1975; Main, 1996). A number of authors have already tried use geological observations to make inferences about past seismogenic clustering behaviour along fault and fracture systems exposed at the surface (e.g. Sibson 1985a; Micklethwaite & Cox 2004, 2006; Kirkpatrick *et al.* 2008). Others have used theoretical approaches such as the use of slip tendency analyses to address this issue (e.g. Collettini & Trippetta 2007). Key questions for structural geologists studying ancient brittle structures are: what might such foreshock-aftershock/earthquake sequences or swarms look like in rocks, why are they diffuse in their distribution and why might they sometimes be kinematically complex?

In this paper, we discuss this problem from a geological perspective, documenting well-exposed examples of zeolite-mineralised factures associated with a linked, distributed system of reverse, strike-slip and extensional faults developed close to the well-known Gole Larghe Fault Zone cutting the Adamello Massif in the Italian Alps. The spatial and geometric diversity of these fractures is shown to result from the hydraulically-assisted reactivation of pre-existing structures occupying at least 0.5 cubic kilometres of the granitic host rocks. We investigate whether, on the reasonable assumption that the fracture sets formed seismogenically, the observed geometric and kinematic relationships represent the geological manifestation of foreshock-aftershock sequences and/or earthquake swarms in an intraplate setting.

2. Regional setting

The Adamello Massif lies in the South Alpine Domain of the Italian Alps and is a tonalitic batholith located near to the intersection of the Giudicarie and Tonale segments of the Periadriatic fault system (Fig. 1a; Bianchi & Dal Piaz, 1937; Bianchi *et al.*, 1970). According to Callegari (1985) and Callegari & Brack (2002), there are four distinct tonalitic–granodioritic intrusions: 1) Re di Castello–Corno Alto; 2) Adamello; 3) Val d'Avio-Val di Genova; 4) Presanella. Geochronological data (Del Moro *et al*., 1983, Hansmann & Oberli, 1991, Viola *et al*., 2001, Mayer *et al.*, 2003 and Stipp *et al.*, 2004) indicate a progressive decrease in the age of these intrusive units from S to N (Re di Castello: 42–38 Ma; Presanella: 32-30 Ma; Pennacchioni *et al.*, 2006). Mineral assemblages preserved in the aureole of the batholith suggest syn-emplacement pressures in the region of 0.25-0.35 GPa, which corresponds to depths in the region of 9-11km assuming typical rock densities (Stipp *et al.* 2004).

The country rocks along the northern border of the Adamello massif were sheared during dextral strike-slip movement of the Tonale Fault (30-32 Ma; Stipp *et al.* 2004; Pennacchioni *et al.* 2006). Post-magmatic, solid-state deformation structures are widely documented in the Val d'Avio-Val di Genova and Presanella plutons and record a progressive down-temperature history of deformation during exhumation of the pluton (Di Toro & Pennacchioni, 2004; Pennacchioni *et al.*, 2006; Mittempergher *et al.*, 2009). These structures include: cooling joints and aplite dykes formed at elevated temperatures (>600°C); conjugate dextral and sinistral ductile shear zones (550-450°C); mainly dextral epidote-chlorite-bearing cataclasites and pseudotachylytes (300-250°C); and late stage zeolite-bearing faults and veins (<200°C) (Pennacchioni *et al.*, 2006). Larger-scale dextral faults and shear zones associated with the development of the main brittle deformation stage (epidote-chlorite-bearing cataclasites and pseudotachylytes) include the NW-SE Passo Cercen Fault Zone in the north together with the E-W to ESE-WNW-trending Gole Larghe Fault Zone (GLFZ) and Lares Fault Zone in the south (Fig 1a). On a regional scale, these structures are viewed as offshoots of the Tonale Fault. The Tonale Fault is also thought by some authors to be cross cut and offset by up to 20km in a sinistral sense by the younger (< 17Ma) Giudicarie Line, the southern part of which forms the eastern boundary of the Adamello plutons (Fig. 1; see Viola *et al.*, 2001).

The rocks of the Adamello pluton arewell exposed in the scoured rock platform where the GLFZ crosses the valley at the toe of the Lobbia Glacier (Figs 1b-c). The host rocks of the Val d'Avio-Val di Genova pluton are typically fine-to medium grained tonalites with a bulk mineralogy: 45-50% plagioclase, 25-30% quartz, 15-20% biotite and 1-5% K-feldspar (Di Toro & Pennacchioni 2004). Many previous studies (e.g. Di Toro & Pennacchioni, 2004, 2005; Pennacchioni *et al.*, 2006; Bestmann *et al.*, 2012; Smith *et al.*, 2013; Mittempergher *et al.*, 2014) have focussed on post-magmatic deformation structures related to the development

of the E-W-trending GLFZ. This structure is made up of a series of E-W trending sub-parallel fault strands, dipping steeply S, which carry abundant cataclasites and pseudotachylytes in a composite fault zone 500-600m thick (Di Toro & Pennacchioni 2005; Smith *et al.*, 2013). Shallowly E-dipping slickenline lineations along the faults and shear sense criteria suggest dextral displacements. ^{39}Ar-^{40}Ar dating of the pseudotachylytes shows that the majority of these friction melts formed ca. 30Ma at depths of 9-11km based on: i) the associated stable fault rock mineral assemblages (K-feldspar-epidote-chlorite); and ii) the preservation of evidence of low temperature plasticity in quartz (Di Toro & Pennacchioni 2004, 2005). These events are broadly coeval with early dextral motions along the Tonale Line (Pennacchioni *et al*., 2006) and pre-date the main phase of exhumation of the Adamello Massif (<22Ma) determined using thermochronology (e.g. Reverman *et al.* 2012).

Despite excellent exposure, the later zeolite-bearing structures in the Lobbia Glacier valley have received little attention. They occur in a variety of orientations and are best exposed in an area covering about 1km^2 over a vertical elevation of at least 500m (including the steep cliffs on either side of the valley) located in the southern, upper part of the GLFZ and its immediate hangingwall rocks (Fig. 1b, c). They belong to a regional suite of late tectonic fracture-hosted zeolite veins and associated alteration zones found throughout the Alps (e.g. see Weisenberger & Bucher 2010). Their precise age is unknown, but it is generally believed that they formed during or following the final exhumation of the Alpine chain, i.e. they are younger than 20Ma and likely developed between 15 and 9 Ma. The depths at which zeolite mineralization developed are uncertain. There is no evidence to suggest that the thermal gradient in the Adamello Massif at this time was significantly greater than its present day value (35ºC km^{-1}). Assuming thermal equilibrium between veins and host rocks, the typical zeolite mineralization temperatures of <200ºC imply maximum formation depths of <6 km. Recent apatite fission track and ^{40}Ar-^{39}Ar dating suggest formation depths

149 of >2.5 km (e.g. Weisenberger et al. 2012). There is no structural evidence for tilting of the
150 Adamello batholith during its exhumation from depth (Brack, 1981).

151

152 **3. Zeolite-bearing structures**

153 *3.1. Field observations*

154 The zeolite mineralization is everywhere associated with linked meshes of
155 anastomosing brittle fractures and veins (Figs 2, 3, 4). Three intimately associated styles of
156 fine to ultrafine grained mineralization are recognized: crystalline vein fills (Figs 2a, b),
157 altered damage zones (Figs 2a, c-e) and mineralized cataclasites and gouges (Figs 2c, d, 3a-
158 d). The zeolites form in a wide variety of bright colours, standing out against the pale greys
159 of the host tonalite, including brick red, milky white, yellow and orange-pale brown (Figs 2,
160 3). Many fault zones and veins preserve evidence of later brittle faulting and cataclasis
161 overprinting and reworking earlier zeolite mineralization (e.g. Figs 5a, b). The broader zones
162 of zeolite-hosted fractures are softer than the host tonalities and are prone to preferential
163 erosion forming breaks of slope (e.g. E-W faults T1, T2, T4; Figs 1b, c, 2f) or gully features
164 that may host melt water streams from the glacier (e.g. faults S1, S3, N1, N2; Figs 1b, 2e).

165 Three main groups of zeolite-bearing faults and fractures are recognised based on
166 differences in orientation (here denoted using strike direction) and shear sense (Figs 1-7): i)
167 NNE-SSW sinistral (Figs 2c, e, 3a, b); ii) NNW-SSE to NNE-SSW normal (Figs 2a, 3c); and
168 iii) E-W sinistral-reverse (Figs 2d, f, 3d). All three fracture sets display local hard linkage
169 (e.g. Figs 2e, f, 3e, f, 4) or are mutually cross-cutting, and contain mineralogically and
170 texturally similar fault rocks (Figs 2-7, Table 1). These observations are consistent with the
171 fracture sets being broadly contemporaneous features. Individual fault and fracture zones are

rarely more than a few centimetres wide and total fault offsets are small (where it can be determined, most are < 1m). The sinistral faults are associated with the largest displacements based on the magnitudes of measured offsets of geological markers, such as igneous contacts, layering or pre-existing faults (e.g. fault S1 shows a maximum 5m offset). Many zeolite-bearing structures reactivate pre-existing shear zones (e.g. Fig 2c). The displacement estimates are therefore likely to represent the *cumulative* displacement history and should be viewed as upper bounds to the slip along the zeolite-bearing structures. The sinistral faults also preserve the greatest widths of associated mineralised and altered damage zones (up to 2m; e.g. faults S1, S2, S3; Fig. 2c, e, 3b).

The NNE-SSW sinistral faults are characterised by the development of laterally continuous tabular volumes, up to 2m wide in map view, that contain fracture meshes associated with zeolite-rich gouge (individually <1cm thick) (Figs 2c, 3a, b), thin zeolite mineral veins (each <1cm wide) (Fig. 3a), shallowly- to moderately-plunging slickenfibre lineations (Fig. 3a) and linked arrays of Riedel (R) and P-shears. The density of zeolite-filled minor faults and fractures decreases moving away from the main faults (Fig. 4).

The N-S normal faults are characterised by the presence of fracture meshes up to 10cm wide (Fig. 2a), finely banded zeolite veins up to 1cm thick and dip-slip slickenfibre lineations (Fig. 3c). A minority of N-S structures show evidence for tensile fracturing with no apparent shearing and fibrous zeolite infills (e.g. Fig. 2b).

The E-W sinistral-reverse faults are more heterogeneous. In many exposures, they are little more than clean breaks containing minor amounts of associated fault rock or mineral fill (e.g. faults T2, T4; Fig. 1b). In contrast, parts of some other E-W faults are characterised by broad regions of brittle fracturing and alteration (damage zones) up to 2m wide, especially in regions close to intersections with NNE-SSW striking sinistral faults, where linked arrays of

196 sinistral-reverse faults locally form duplex-like structures (e.g. faults T1, T3; Figs 2d, f, 3d).
197 In fault T1, the thickness of the damage zone tapers down from 2 meters to 10 cm in just few
198 tens of meters moving away from the intersection with the main NNE-SSW striking sinistral
199 fault S1 (Fig. 4). Shear surfaces locally carry zeolite-dominated gouge and cataclasite (Figs
200 2d, 3d), oblique-slip slickenfibre lineations and R shears (Figs 3d). The footwalls of the
201 larger E-W faults (T1, T3) are locally hard linked to sub-vertical N-S trending tensile fracture
202 systems (up to 2 cm wide) filled with injected orange-brown zeolite gouge and, locally,
203 breccia (e.g. see Fig. 6a-d) that extend several metres down into the immediate footwall
204 rocks.

205 In summary, three kinematically distinct hard-linked and mutually cross-cutting fault
206 sets and fracture meshes are associated with syn-deformational zeolite mineralization in the
207 Lobbia Glacier valley. The NNE-SSW striking sinistral faults mostly re-activate small
208 sinistral mylonitic shear zones. A proportion of the cumulative displacement might have been
209 accommodated during slip along the mylonitic shear zones at ~500°C. As a consequence, the
210 cumulative slip associated to the zeolite-facies deformation (< 200°C) event is difficult to
211 constrain with precision. However, the NNE-SSW striking sinistral faults are interpreted as
212 the master faults because: (1) they are associated with the thickest zones of zeolite
213 mineralization; and (2) the damage zone thicknesses of the E-W striking faults decreases
214 moving away from where they intersect with the NNE-SSW striking faults (Fig. 4).

215 *3.2. Mineralogical and microstructural observations*

216 Regardless of movement sense, all fault rocks, alteration zones and mineral fills are
217 associated with the same zeolite mineralization. This compositional consistency was verified
218 using X-ray diffraction analysis (Table 1, Appendix 1). The main mineral cements found
219 were zeolites (Ca-rich stilbite, scolecite and stellerite, together with the Na- and Ca-rich

laumontite) and prehnite. Such a mineral assemblage is typical of precipitation from CO_2-poor, alkaline-rich aqueous fluids at T < 200°C and P < 200MPa (Deer et al., 1992; Weisenberger & Bucher 2010, 2012). Fluid-rock interactions are evident from the observed widespread alteration of host plagioclase feldspars, with many zeolite-hosted veins, fault zones and fractures displaying pale alteration haloes up to several cm thick (e.g. Figs 2a, d, 3b, 5b).

Many N-S and NNE-SSW structures seem to develop initially as tensile/hybrid fractures hosting composite zoned zeolite veins (e.g. Figs 2b, 3a, 5a, 5b), with anhedral zeolites at the vein walls and fine-grained acicular zeolites towards the centre (Fig. 7a). Crack-seal textures are locally preserved and are consistent with repeated fluid flow events during fracturing (e.g. Cox 1987; Sibson *et al.*, 1988; and Hilgers & Urai 2005). Once formed, these tensile veins are widely overprinted by shearing events forming a zeolite-cemented cataclasite/gouge with clasts of earlier zeolite vein material (Figs 5b, 7b). Progressive shearing leads to the destruction of the vein clasts producing fine- to medium-grained cataclasites (Figs 5b, 7c). The preservation of clasts of zeolite cataclasite suspended in fine grained zeolite gouge also suggests that repeated shearing events have occurred along some larger faults with many of these cataclasite clasts displaying well-developed haloes of crystalline zeolite consistent with growth into a fluid-filled cavity (Fig. 7d). Following cementation, many N-S and NNE-SSW shear fractures have also been reopened as tensile fractures filled with new crystalline zeolite (Fig. 7e). E-W faults do not host widespread tensile veins and tend to carry either zeolite mineralized cataclasite and gouge (e.g. Figs 2d, 3d), or to be clean breaks (e.g. Fig. 2f). One feature spatially associated with some larger E-W faults (e.g. T1, T3) is the presence of zeolite gouge injections both into the host rocks along sub-vertical N-S fractures and internally within fault zones cross-cutting earlier gouges/cataclasites (Figs 6a-c, 7f).

In summary, the faults and fractures have clearly hosted significant aqueous fluid flow during their history leading to the observed zeolite mineralization and alteration of the immediately adjacent tonalite host rocks. They typically preserve a history of one or more cycles of fracturing and cataclasis followed by cementation and sealing possibly related to fluid pressure fluctuations during deformation. N-S and NNE-SSW structures carry widespread tensile or hybrid veins fills that are either overprinted by later shearing or reactivate pre-existing shear fractures.

3.3. Evidence for seismogenic behaviour during formation of zeolite-bearing brittle structures

Petrographic, microstructural, geochemical and stable isotopic analyses (e.g. Pennacchioni *et al*., 2006; Smith *et al*. 2013; Mittemperger *et al*. 2014) have shown that the first ingress of crustal metamorphic fluids in the Adamello Massif occurred *prior* to the zeolite mineralization during dextral cataclastic faulting along the GLFZ. The widespread preservation of pseudotachylytes associated with these E-W faults demonstrates the repeatedly seismogenic nature of the fault zone at that time (e.g. see Di Toro & Pennacchioni 2004, 2005). Equivalent geological indicators of seismic slip (cf. Cowan 1999; Niemeijer *et al.* 2012) are not associated with the zeolite-hosting fault movements. Nevertheless, there is other geological evidence to suggest that at least some of the zeolite-bearing fault displacements were seismogenic. Zeolite-mineralized gouge injections along N-S tensile fractures are observed linking up into two of the largest E-W sinistral-reverse faults in the area (T1, T3, see Figs 6a-c, f). Earthquake events can rapidly amplify fluid pressures along faults for short time periods (e.g. Nur and Booker, 1972) leading to the fluidization and local injection of unconsolidated fault gouges (e.g. see Sibson, 1993; Smith *et al.* 2008; Rowe *et al.* 2012). In the following section, we investigate the relationships between stress, variations in

fluid pressure and possible seismogenic slip to explain the observed kinematic diversity of zeolite-bearing structures.

4. Palaeostress analysis, fault reactivation potential and Coulomb stress modelling

We analysed the reactivation potential of pre-existing structures with different orientations in the Lobbia Glacier valley in three stages:

i) The slickenline data measured from the three different fault sets (NNE-SSW sinistral, N-S normal and E-W sinistral-reverse) were used to infer the orientations of the principal palaeo-stresses during the formation of the zeolite-bearing structures, using standard stress inversion techniques (following Delvaux & Sperner, 2003, Fig. 9).

ii) The potential effects of elevated differential stresses and pore-fluid pressures on the stability of reactivated structures were examined using a slip and dilation tendency analysis (following Ferrill *et al*. 1999; Lisle & Srivastava 2004) (Fig 10a, b).

iii) Finally, we undertook Coulomb stress transfer modelling (following Lin & Stein 2004; Toda *et al.* 2005) to determine whether the observed kinematic diversity amongst the zeolite-bearing structures can be explained by static loading (stress transfer) following seismogenic slip along the main NNE-SSW sinistral structures.

4.1. Palaeostress analysis

Stress inversion techniques allow modelling of the stress tensor associated with a set of coeval and consistent kinematic indicators (e.g. slickenlines) measured on a set of fault surfaces. The fundamental assumption in all stress inversion techniques (Wallace, 1951; Bott, 1959) is the statistical parallelism between the observed slip vector (measured on fault surfaces) and the model shear traction (shear component of stress tensor, resolved on a

292 particular fault plane via Cauchy's double dot product). This assumption is reasonable if the
293 fault displacements are small (infinitesimal strain and no rotation), a condition met by the
294 small-displacement zeolite-bearing structures considered here.

295 Several graphical and numerical approaches have been proposed (e.g. Angelier and
296 Mechler, 1977; Etchecopar *et al*., 1981; Angelier, 1991; Michael, 1984; Reches, 1987;
297 Yamaji, 2000; Delvaux & Sperner, 2003). In most cases, the solution is obtained as a reduced
298 stress tensor with just four parameters (Etchecopar *et al.*, 1981): the orientation of the three
299 principal axes and the shape factor $\delta = (\sigma_2 - \sigma_3) / (\sigma_1 - \sigma_3)$. This tensor represents, in a-
300 dimensional form, the deviatoric component of the total stress tensor; the isotropic
301 component does not influence shear stress on fault surfaces. Ideally, the most robust
302 numerical solution requires at least four statistically independent fault sets to be measured
303 (see Angelier, 1991). In the case of the zeolite-bearing faults, this condition is met since we
304 have the three fault sets discussed above, plus a few faults in other scattered orientations.

305 Our modelling was performed using the Win Tensor software (Delvaux & Sperner,
306 2003). The inversion of the total zeolite-bearing fault and fracture dataset (Fig. 9) obtains a
307 wrench tectonic regime with σ_1 approximately horizontal N-S, σ_3 approximately horizontal
308 E-W, and σ_2 sub-vertical. The shape factor δ is 0.8, meaning that σ_2 is closer to σ_1 rather than
309 σ_3. We also carried out analyses on smaller sub-sets of the total data located, for example,
310 inside and outside the GLFZ. This had little effect on either the nature or orientation of the
311 modelled principle stresses, leading us to conclude that despite the obvious scatter in
312 fault/fracture orientations (Fig. 9), the regional stress field at the time of faulting was
313 generally fairly consistent in orientation.

314 The Mohr circle plot showing the normal and tangential components of the stress
315 tensor resolved on each fault surface (Fig. 9) demonstrates that the NNE-SSW sinistral and

316 N-S normal faults are reasonably well oriented for slip as they fall in the hybrid
317 shear/opening field, while the E-W faults are strongly misoriented (Sibson, 1985b) since they
318 are characterized by high normal and low shear stresses. The plots also show that there are no
319 Andersonian faults in our datasets, a conclusion consistent with the field and microstructural
320 observations, which indicate that most brittle faults reactivate structures formed during
321 previous deformation phases.

322 The tectonic regime obtained from this analysis accords well with other results
323 obtained for this part of the Alps in the Miocene (17-7Ma, e.g. Prosser, 1998; Castellarin *et*
324 *al.*, 2006, Agliardi *et al.*, 2009), where the main regional-scale system is represented by the
325 NNE-SSW sinistral Giudicarie Fault System that lies to the east of the Adamello Massif (Fig.
326 1a; Prosser 1998; Viola *et al*. 2001). Similarly orientated brittle sinistral faults are also known
327 to offset exposed segments of the Tonale Fault by up to 600m (e.g. see figure 2 in Stipp *et al.*
328 2004). We therefore conclude that the zeolite-bearing fault structures in the Lobbia Glacier
329 valley belong to a regionally recognized late fault system of probable Miocene age.

330 *4.2. Slip tendency and dilation tendency analyses*

331 A slip and dilation tendency analysis is appropriate in the case of the zeolite–bearing
332 faults of the Lobbia Glacier valley since reactivation is almost invariably observed, meaning
333 that the pre-existing faults are likely to be significantly weaker than the intact tonalite. Slip
334 tendency (Morris *et al.*, 1996), and particularly normalized slip tendency (Lisle and
335 Srivastava, 2004), defined as $NST = \tau/\sigma_n/\mu$, (the shear to normal stress ratio on a given
336 fault or fracture surface, normalized by the friction coefficient) represents the proneness to
337 slip of that particular structure. Thus critically stressed Andersonian faults show NST = 1,
338 whilst surfaces parallel to a principal plane of the stress tensor, with zero shear stress, have
339 NST = 0 (Bistacchi *et al.*, 2012).

340 Dilation tendency is defined as $DT = (\sigma_1 - \sigma_n)/(\sigma_1 - \sigma_3)$, where σ_n is the normal
341 stress acting on a particular structure. This represents the proneness of a fracture with a given
342 orientation to open under an imposed fluid pressure (Ferrill *et al*., 1999). In Figure 10a and b,
343 both NST and DT are colour-coded on the stereoplot for the proposed regional stress regime
344 (Fig. 9c), and poles corresponding to typical attitudes of NNE-SSW, N-S and E-W faults are
345 highlighted. In addition, the MATLAB® Toolbox of Bistacchi *et al.* (2012) allows the
346 prediction of the orientation of theoretical Andersonian surfaces, which are also shown.

347 The hypothetical Andersonian faults predicted by the analysis are not recognized in
348 the field. As a result of their high DT values, the NNE-SSW and N-S structures are likely to
349 open as soon as the fluid pressure overcomes σ_3, and thus these structures are able to behave
350 as very effective preferential fluid circulation pathways. Once a fracture network or mesh is
351 established, fluid pressure can rise to higher levels, at least locally and episodically. The N-S
352 structures also have high NST values (despite being non-Andersonian), so they are the most
353 likely to be reactivated amongst the pre-existing structures. Conversely, the E-W faults have
354 low NST and DT values, and therefore require higher fluid pressure to be activated in slip,
355 and also to open and be infiltrated by fluids. Sub-vertical N-S veins show the highest DT
356 (almost 1), in agreement with the field and microstructural observations that these tensile
357 veins (e.g. Fig. 2b, 6b, c) are the only possible newly formed (as opposed to reactivated)
358 structures developed under these stress conditions. They potentially formed as tensile
359 hydraulic fractures when the fluid pressure exceeded σ_3 plus the tensional strength of the
360 intact tonalites.

361 *4.3. Coulomb stress modelling*

362 Following the pioneering studies of Reasenberg & Simpson (1992), King *et al.* (1994)
363 and Stein *et al.* (1997), it is now well known that the variable slip distribution on a fault

364 during an earthquake results in an heterogeneous strain field in the wall rocks. This in turn,
365 can produce elastic stresses that perturb the regional stress field, resulting in an increased or
366 decreased possibility of failure on nearby faults. Such a *stress transfer* process is now
367 commonly invoked in order to explain earthquake triggering (on already critically-loaded
368 faults) and might also plausibly play a role in the development of the zeolite-hosting fracture
369 systems of the Lobbia Glacier valley.

370 The longest and possibly largest displacement fault in the area is the NNE-SSW
371 trending sinistral structure located in the centre of the Lobbia Glacier valley (fault S1; Figs
372 1b, c). It shows a maximum sinistral offset of 5 metres (based on offset igneous markers)
373 close to the toe of the Lobbia Glacier, decreasing northwards to <2 metres where it offsets
374 fault T1 (Fig. 3f). Whilst the *ca.* 5 m offset may include displacements along pre-existing
375 sinistral mylonitic shear zones, the *ca.* 2 m offset of fault T1 can be confidently associated
376 with the zeolite-associated faulting episode (Fig. 4). Further to the north, fault S1 branches
377 into two zones of increasingly small offset, linked strike-slip and normal fault segments that
378 die out close to fault T4 (Fig. 1b). This overall northwards decrease in offset magnitude is
379 consistent with northward fault propagation of a fault tip zone. Using the methods of Lin &
380 Stein (2004), King *et al.* (1994) and Toda *et al.* (2005), we use the Coulomb 3.2 stress
381 modelling code within MATLAB® (http://earthquake.usgs.gov/research/modeling/coulomb/)
382 to estimate the static stress changes resulting from an hypothetic sinistral "mainshock"
383 rupture along fault S1.

384 Assuming a depth of 4 km, we model a single hypothetical rupture on the fault S1
385 approximately equivalent to an M = 3 earthquake (0.2 m maximum slip at the toe of the
386 Lobbia glacier in the south, tapering to 0 m at the northern tip of the fault). A slip scenario of
387 this kind results in a transient, localized near-field stress perturbation in the vicinity of the
388 fault (Fig. 11a). The distribution of stress concentrations generated by slip on S1 (represented

as Coulomb stress change resolved onto fault surfaces with the same orientation as the reactivated E-W structures, taken as 100/50 S) matches well with the distribution of the reactivated thrust segments observed in the field (Figs 11a,b). To test the resolved direction of slip on E-W faults that could be triggered by rupture (or repeated ruptures) on S1, we inserted 3 synthetic E-W faults (coincidental with T1, T2 and T3) and calculated the most likely rake direction during failure. From this calculation the E-W faults would be expected to fail with as sinistral-reverse faults with a rake of 55^0 (Fig. 11c) almost exactly matching the slickenline lineations measured in the field (see Fig. 8). The stress transfer model also explains the changes in damage zone thickness of the larger E-W faults such as fault T1, which is up to 2 m adjacent the largest NNE-SSW fault, gradually decreasing to almost zero 250m along strike and away from the fault intersection (Fig. 4). Similar along-strike variations in displacement can be also accommodated by secondary displacements along the smaller N-S-trending normal faults located in the hangingwall regions of the E-W faults (Fig. 11d). Note that thrust and normal fault displacements would be necessarily limited since they would have rapidly dissipated the local stress perturbation, and the system would have reverted to the homogeneous far-field regional stress field in which the E-W structures were once again stable.

The model presented in Figure 11a examines the stress transfer that could occur during a single small rupture event along the fault S1. Given the field and microstructural evidence for multiple fracture and associated mineralization episodes, it seems probable that repeated rupturing events, each with a potential associated stress transfer will have occurred. It is also possible that other large N-S faults (e.g. S2, S3) have hosted mainshock rupture events at some time in their history. The preservation of injected gouges in the footwalls of faults T1 and T3 suggests that once these faults were sufficiently loaded, they also failed seismically, but we have chosen to not model the stress transfers associated with slip along

these E-W faults as we are unable to constrain their finite displacements due to a lack of offset markers.

4.4. Summary

The analyses presented above suggest that reactivation of the pre-existing, generally N-S-trending structures (NNW-SSE sinistral, N-S normal faults) within the inferred regional stress field is plausible particularly when assisted by the development of elevated differential stresses and/or pore-fluid pressures. The sinistral-reverse kinematics observed along the zeolite-bearing E-W faults are consistent with the predictions of Coulomb stress transfer following slip along the main N-S structures. In the following discussion, we address the possible relationships between deformation, pore pressure variation and the timescales of fracturing within the *ca*. 0.5 km^3 rock volume surrounding the main N-S structures.

5. Discussion

5.1. Changes in pore fluid pressure and stress

The forgoing description and analyses show that in the area of the Lobbia Glacier valley, a kinematically diverse set of coeval zeolite mineralised faults and veins with various orientations are spatially associated with the upper part and immediate hangingwall of the older GLFZ. The observed mineralization and associated alteration of the tonalite wall rocks requires the ingress and throughput of significant volumes of aqueous, low temperature (<200°C) alkaline fluids (see Weisenberger & Bucher 2010 and references therein). This fluid flow has clearly been facilitated by brittle fracturing and fault reactivation. So how might these processes be related?

436 It is well known that failure along faults may be driven by either increases in shear
437 stress during the seismic cycle (stress-driven faulting), or by increases in pore fluid pressure
438 leading to hydrofacture (hydraulically-driven faulting) or by some intermediate combination
439 of these end-member controls (e.g. Phillips 1972; Sibson 1981; Cox 2010). A key observation
440 made both in the field and thin section is that many N-S and NNE-SSW shear fractures also
441 opened periodically as tensile or hybrid fractures and veins (e.g. Figs 2b, 3a, 5a). This
442 requires the development of elevated fluid pressures and hydrofacturing on the reasonable
443 assumption that the zeolite-bearing fracture systems formed at depths > 1-2km (Cox 2010).

444 In a hydraulically-driven scenario where the differential stresses remain constant an
445 increase in pore fluid pressures will reduce all the effective compressive principal stresses by
446 an amount equal to the fluid pressure assuming that poro-elastic effects (Nur & Byerlee 1971)
447 are negligible. Mohr circles are translated to the left and can ultimately strike the failure
448 envelope leading to failure (e.g. see Twiss & Moores 1992; Zoback 2007; Jaeger *et al.* 2007).
449 The field and microstructural observations show that the formation of the majority of N-S and
450 NNE-SSW tensile fractures is typically followed by frictional sliding and cataclasis (shear
451 fracture) during either sinistral or normal fault movements on NNE-SSW and N-S trending
452 structures, respectively. It is self-evident that more modestly elevated pore fluid pressures
453 would be required in order for shear failure to occur along suitably oriented cohesionless
454 fractures.

455 It seems unlikely that changes in fluid pressure alone caused the observed fracturing
456 associated with the zeolite mineralization since this cannot explain how the unfavourably
457 oriented E-W structures were reactivated at the same time as the NNE-SSW and N-S
458 structures. Furthermore the recognition of tensile, hybrid and shear fracturing events along
459 the NNE-SSW and N-S structures points to variations in the magnitudes of the differential

460 stress with time. The possible relationships between stress-driven seismogenic faulting, fluid
461 flow and mineralization are now examined and discussed.

462 *5.2. Timescales for seismogenic faulting*

463 Our findings are consistent with an initial hypothesis that the geometric and kinematic
464 relationships preserved within the zeolite-bearing structures of the Lobbia Glacier valley
465 represent a plausible geological analogue for foreshock-aftershock sequence and/or
466 earthquake swarm complexity. Several examples of natural earthquake swarms and/or
467 foreshock-aftershock sequences have been ascribed to the presence and/or migration of pore
468 fluids or magma under elevated pressures. Miller *et al.* (2004), for example, describe an
469 example from the Umbria-Marche region of the northern Apennines in Italy where an
470 aftershock sequence was interpreted to have been triggered by the presence of elevated pore
471 fluid (CO_2) pressures at depth which led to the failure of apparently stable, moderately-
472 dipping normal faults. Rupture of this fault system is considered to have allowed the over-
473 pressured fluid to move progressively up-dip, destabilizing individual fault segments as it
474 migrated. This migration and the failures it induced were recorded as a complex sequence of
475 migrating aftershocks. Such earthquake clusters are often characterised by multiple seismic
476 events closely spaced in time and location, with highly variable earthquake focal
477 mechanisms, especially for the smaller events (e.g. Mogi, 1963; Scholz, 2002; Shearer et al.
478 2003; Kassaras et al., 2014). There are also many examples of similarly complex induced
479 seismicity resulting from human activities where fluids have been injected into the crust
480 during shale-gas exploration, geo-sequestration or enhanced geothermal exploitation (e.g.
481 Raleigh et al., 1976; Seeber et al., 2004; Deichmann & Giardini, 2009; Baisch et al., 2006;).
482 A key question, therefore, is to assess whether pore pressure diffusion through the *ca*. 0.5
483 km^3 rock volume cut by kinematically-diverse zeolite-bearing structures in the Adamello
484 Massif is consistent with the timescales associated typical earthquake foreshock, aftershock

485 or swarm sequences. We use the mainshock model along the NNE-SSW-striking sinistral
486 fault to test whether an increase in pore fluid pressure generated in the immediate vicinity of
487 a rupture would be able to diffuse out through a fracture system over the timescales of a
488 typical aftershock sequence.

489 The timescale, τ, for any diffusive process is given by:

490 $$\tau = \frac{l^2}{\kappa} = \frac{(\phi\beta_f + \beta_r)\eta l^2}{k}, \qquad (3)$$

491 where l = diffusion distance; κ = hydraulic diffusivity; ϕ = porosity; β_f = fluid
492 compressibility; β_r = rock compressibility; η = fluid viscosity; k = permeability (e.g.
493 Townend and Zoback, 2000; Wibberley, 2002). The studied zeolite-bearing structures seem
494 to cluster within *ca*. 0.5 km^3 of the main NNE-SSW trending sinistral fault (Fig. 1b),
495 implying that a diffusion distance ≤ 1000 m is appropriate. Figure 12 shows the timescales
496 for a pore pressure anomaly to diffuse distances between 100 and 10000 m, assuming a range
497 of hydraulic diffusivities κ. Clearly there is a large (*ca.* 7 orders of magnitude) variation in
498 reported or estimated hydraulic diffusivities. However, given the small displacements
499 observed along the zeolite-bearing faults in this part of the Adamello massif we suggest the
500 most appropriate diffusivity values to use here are those derived from: (1) static permeability
501 measurements of small (< 1 m) displacement, zeolite-bearing faults in crystalline basalt
502 (Walker *et al.*, 2013a, b); and (2) estimated *in situ* permeabilities for intraplate crust
503 (Townend and Zoback, 2000). These hydraulic diffusivities lie within the range 0.02 to 0.2
504 m^2s^{-1}, giving characteristic diffusion timescales of 13 to 6600 days (0.04 to 18 years) over a
505 distance of 0.5 to 1 km (Fig. 12). Although imprecise – and adopting a steady, constant
506 hydraulic diffusivity is a significant over-simplification – the timescales associated with
507 hydraulic diffusivities toward the upper end of this range are consistent the timescales

associated with aftershock or other temporally-clustered earthquake events likely to have been significantly influenced by fluid diffusion (e.g. Chen *et al.* 2012).

5.3. Fluid influx and cyclic reactivation model

The analyses presented above demonstrate that the brittle reactivation of a cluster of differently oriented pre-existing structures and the associated zeolite mineralisation can be explained by seismogenic fracturing processes in the presence of an at least locally overpressured fluid in the Adamello Massif. In the following section, we propose a highly simplified conceptual model.

i) Initial fluid ingress: The detailed study of fracturing associated with the dextral GLFZ carried out by Smith *et al.* (2013) suggests that, prior to zeolite mineralization, the rocks of the Adamello Massif adjacent to and especially within the GLFZ were likely to have been impermeable. These authors have documented pervasive fluid-rock interaction leading to development of a 200m thick zone of K-feldspar-epidote-chlorite alteration and veining centred on the core of the GLFZ (Fig. 1b). Up to 85% of the observed microfractures in this zone are sealed by these minerals.

In order to introduce the zeolite-mineralizing fluid required by our field and microstructural observations, we follow Yardley (1997) in suggesting that the fluid pressure in the low permeability tonalities was initially sub-hydrostatic. Mineralising fluids must have been drawn into these crystalline rocks by early tectonically-induced rupturing along deeply penetrating brittle fractures such as the larger displacement NNE-SSW sinistral fault set (Fig. 13). If early zeolite mineralisation followed initial fluid ingress, this would trap fluids and promote the development of fluid overpressures within the fractures (cf. Sleep & Blanpied 1992). It also seems likely that the steeply south-dipping, pre-existing alteration zone centred on the GLFZ would have acted as an impermeable barrier helping to further trap and

overpressure the zeolite-bearing fluids. Given the observed preferential development of this mineralisation in the immediate hangingwall and upper part of the GLFZ, we suggest that the fluids may have been drawn either vertically down or laterally from the south into position. This proposal could plausibly be tested using stable isotopic analyses to test whether the fluids associated with mineralization have a meteoric signal consistent with derivation from a near surface source.

ii) Cyclic seismogenic faulting, fluid-assisted rupturing and mineralisation: we propose that a series of "mainshock" ruptures occurred along one or more of the large NNE-SSW sinistral faults – such as fault S1 (Figs 13i,iv,vii) leading to an increase in pore fluid pressure in the upper part of the GLFZ immediately adjacent to the pre-existing impermeable zone of alteration. We suggest that fluid migration and/or pressure diffusion away from the main rupture transiently led to increases in local pore fluid pressure (Figs 13ii, v, viii). Depending on the state of differential stress, this could have led to aftershock slip events due to hydraulic tensile/hybrid fracturing (low differential stress) or to hydraulically-assisted shear fracturing (high differential stress) along pre-existing NNE-SSW strike-slip and N-S normal faults (Figs 13ii, v, viii). Multiple mainshock rupturing events would also lead to stress transfer and periodic partial reactivation of the adjacent E-W faults in the GLFZ. Following each mainshock rupture, differential stresses and perhaps pore fluid pressures would likely fall, meaning that the majority of the pre-existing structures once again became stable. Any decrease in pore fluid pressure would also lead to zeolite precipitation (Figs 13iii, vi, ix). This would effectively seal the faults and allow elevated fluid pressures to begin to develop again either due to further influx of fluids and/or due to repeated seismic mainshocks along the larger NNE-SSW fault(s) re-starting the rupture-reactivation-cementation cycle (Figs 13i-iii, iv-vi, vii-ix; cf. Sibson et al. 1995).

556 It is not unreasonable to suggest that every fracture-forming event in crystalline rocks
557 of the Adamello Massif had the capacity to produce a small earthquake, be it a stress- or
558 fluid-driven process. Having produced a model to account for the spatial and temporal
559 clustering of fractures in the *ca.* 0.5 km^3 of rock located close to the GLFZ in the Lobbia
560 Glacier valley, we used MyFault™ software to generate synthetic earthquake focal
561 mechanisms for illustrative purposes, using fault surfaces as principal nodal planes and
562 kinematic data to reconstruct the auxiliary plane.

563 Using the deformation sequence described in this paper and the synthetic earthquake
564 focal mechanisms, Figures 13i-ix schematically illustrate a hypothetical aftershock sequence
565 leading to reactivation of the zeolite-hosting structures in the Adamello Massif. Note that the
566 relative magnitudes of the aftershocks shown are purely schematic as these are unconstrained.
567 For instance, both the NNE-SSE striking faults and the E-W faults given their dimensions
568 could produce the main shocks of an earthquake sequence hosted in the investigated rock
569 volume. However, the field evidence discussed earlier suggests that the NNE-SSW faults
570 hosted the main (sinistral strike-slip) seismic ruptures. It is these faults that were most
571 favourably oriented with respect to the inferred late Miocene regional stress tensor of this
572 sector of the Southern Alps. As a consequence, though seismic faulting occurred along strike-
573 slip, normal and transpressive faults in the area, only the major ruptures were consistent with
574 the regional stress. This is similar to many foreshock/mainshock/aftershock sequences and
575 swarms. For instance, in the case of the 2011 Oichalia (Greece) swarm, the main shocks ($3 <$
576 $M_w < 4.8$) have focal mechanism (normal) consistent with the stress field (extensional) of the
577 area (Kassaras *et al.*, 2014). By contrast, the few interpretable focal mechanisms of the
578 smaller earthquakes ($M_w < 3$) are scattered, and include strike-slip and reverse mechanisms.
579 The evolution of this swarm was probably controlled by fluid migration along the main
580 extensional structures (Kassaras *et al*., 2014). In general, normal faults and strike-slip faults

are more permeable given their lower mean stress allowing fluid ingression, which then significantly influences the earthquake sequence evolution.

The sequence we describe is also comparable to the earthquake sequence observed in New Madrid in 1811-1812 (Mueller *et al.*, 2004) albeit on different length scales. Here rupture on the NE trending Cottonwood Grove Fault (dextral strike-slip) led to stress-loading upon and subsequent failure of the SW-dipping Reelfoot Thrust. Our modelled earthquake swarm shows a spatially distributed and complex mixture of focal mechanisms that is also similar to the cloud of focal mechanisms observed for the more recent (1974-2006) micro-seismicity in the New Madrid region (Mueller *et al*., 2004; Shumway, 2008).

6. Conclusions

1) Small displacement late brittle fractures hosting zeolite mineralisation form a diffuse array of structures in the upper part and immediate hangingwall of the GLFZ in the Lobbia Glacier valley. Formed due to the ingress of aqueous alkaline fluids at <200°C, and at depths of 2.5-6 km, we have shown that the locations and geometries of the mineralized fractures are controlled by the distributed presence of pre-existing structures formed during the earlier history of the Adamello pluton and GLFZ.

2) Geological observations and stress analyses suggest that favourably orientated pre-existing NNE-SSW and N-S structures were initially reactivated under stress loading and/or transiently high pore fluid pressure conditions developed adjacent to a pre-existing highly cemented low permeability barrier located in the core of the GLFZ. Once formed, these fractures were then susceptible to repeated reactivation as both shear and tensile fractures.

3) Coulomb stress modelling shows that repeated fluid-assisted seismogenic rupturing along the main NNE-SSW sinistral fault(s) plausibly led to stress transfer and loading of previously stable pre-existing E-W structures of the GLFZ which were reactivated as sinistral-reverse faults. Seismogenic movements induced localised fluid over-pressurization leading to further tensile fracturing and injection of fluidized zeolite-bearing gouges. The interaction between the NNE-SSW sinistral faults and E-W sinistral-reverse faults also may have led to further accommodation movements along linked N-S trending normal faults.

4) Decreases in stress and/or pore fluid pressures following rupture events and the formation of fracture meshes appear to have led to system locking and cementation by zeolite mineralization. This would have reduced the efficiency of fluid migration, allowing elevated fluid pressures to be re-established thus helping to restart the "rupture-reactivation-cementation" cycle.

5) We propose that the reactivated mineralized structures associated with the GLFZ represent a vivid geological manifestation of multiple ancient earthquake clusters – perhaps a series of mainshock-aftershock events (as illustrated schematically in Figure 13). Their kinematic complexity is clearly shown to result from the reactivation of pre-existing structures in a wide range of orientations.

6) Our findings illustrate the importance of fluids and reactivation in upper crustal seismogenic faulting processes and provide useful geological constraints that allow a better understanding of the complex geological manifestations of natural earthquakes at depth.

Acknowledgements: The authors would like to thank Tom Mitchell, Jean Pierre Gratier, Steve Smith, Silvia Mittempergher, Angela Castagna, Marieke Rempe, Marie Violay, Michele Fondriest, Andrea Zanchi, Matteo Massironi and, Nicola DePaola for discussions and help during fieldwork. Federico Zorzi is thanked for XRD analysis and Leonardo Tauro

628 and Elena Masiero for thin section preparation. The financial and scientific support of the
629 Leverhulme Trust (to Holdsworth), Durham University and of the European Research
630 Council Starting Grant USEMS No. 205175 (to Di Toro) are warmly acknowledged. Stephen
631 Cox, Andrea Billi, Steve Micklethwaite and Anonymous are thanked for their reviewers
632 comments. Stress inversion was performed with Win Tensor, courtesy of Damien Delvaux
633 (http://www.damiendelvaux.be/Tensor/WinTensor/win-tensor.html). Coulomb stress
634 modelling was performed using "Coulomb 3" software, courtesy of USGS and partners
635 (http://earthquake.usgs.gov/research/modeling/coulomb/).

636

637 **References**

638 Agliardi, F., Zanchi, A., Crosta, G.B., 2009. Tectonic vs. gravitational morphostructures in
639 the central Eastern Alps (Italy): Constraints on the recent evolution of the mountain range.
640 *Tectonophysics* **474,** 250–270.Anderson, E. M. 1951. *The Dynamics of Faulting*. (2nd Edn)
641 Oliver & Boyd, Edinburgh.

642

643 Angelier, J., 1991. Inversion directe de recherche 4-D: comparaison physique et
644 mathématique de deux méthodes de détermination des tenseurs des paléocontraintes en
645 tectonique de failles. *Compte Rendus l'Académie des Sci. Paris* **312,** 1213–1218.

646

647 Angelier, J., Mechler P., 1977. Sur une méthode graphique de recherche des constraintes
648 principale également utilisable en tectonique et en seismologie: la méthode des dièdres droits.
649 *Bulletin de la Société Géologique de France*, **7**, 1309-1318.

650

651 Baisch, S., Weidler, R. Voros, R., Wyborn, D., de Graaf, L. 2006, Induced Seismicity during
652 the Stimulation of a Geothermal HFR Resevior in the Cooper Basin, Australia, *Bulletin of the*
653 *Seismological Society of America*, **96(6)**, 2242-2256.

654

655 Bestmann M., Pennacchioni G., Nielsen S., Göken M., de Wall H. 2012. Deformation and
656 ultrafine dynamic recrystallization of quartz in pseudotachylyte-bearing brittle faults: A
657 matter of a few seconds. *Journal of Structural Geology*, **38**, 21-38.

658

659 Bianchi A., Dal Piaz, G.B. 1937. Atlante geologico-petrografico dell'Adamello meridionale;
660 regione fra lo Stabio ed il Caffaro. *Mem. Ist. Geol. Min. Univ. Padova*, **12**, 1–16.

661

Bianchi A., Callegari, E., Jobstraibizer, P.G. 1970. I tipi petrografici fondamentali del plutone dell'Adamello (tonaliti, quarzodioriti, granodioriti e loro varietà leucocrate).*Mem. Ist. Geol. Min. Univ. Padova*, **27**,1–148.

Bistacchi, A., Massironi, M, Menegon, L., Bolognesi, F., Dongi,V. 2012. On the nucleation of non-Andersonian faults along phyllosilicate-rich mylonite belts. In: Healy, D., Butler, R. W. H., Shipton, Z. K. & Sibson, R. H. (eds) *Faulting, Fracturing and Igneous Intrusion in the Earth's Crust*. Geological Society, London, Special Publications, **367**, 185–199. http://dx.doi.org/ 10.1144/SP367.13

Bott, M.H.P., 1959. The mechanisms of oblique slip faulting. *Geological Magazine,* **96,** 109–117.

Brack, P., 1981. *Structures in the southwestern border of the Adamello intrusion.* Schweizerische Mineralogische und Petrographische Mitteilungen 61, 37–50.

Callegari E. 1985. *Geological and petrological aspects of the magmatic activity at Adamello (northern Italy)* Memorie della Società Geologica Italiana, **26,** 83–103

Callegari E., Brack P. 2002. *Geological map of the Tertiary Adamello batholith (Northern Italy) -Explanatory notes and legend.* Memorie di Scienze Geologiche, **54**, 19–49

Castellarin, A., Vai, G.B., Cantelli, L., 2006. The Alpine evolution of the Southern Alps around the Giudicarie faults: A Late Cretaceous to Early Eocene transfer zone. *Tectonophysics* **414,** 203–223.

Chen, X., Shearer, P.M., Abercrombie, R.E., 2012. Spatial migration of earthquakes within seismic clusters in Southern California: Evidence for fluid diffusion, *Journal of Geophysical Research,* **117,** doi: 10.1029/2011JB008973.

Chung, F.H. (1974) Quantitative interpretation of X-ray diffraction patterns of mixtures. II. Adiabatic principle of X-ray diffraction analysis of mixtures. *Journal of Applied Crystallography*, **7,** 526–531.

Collettini C., Trippetta F 2007. A slip tendency analysis to test mechanical and structural control on aftershock rupture planes. *Earth and Planetary Science Letters*, **255**; 402-413, doi: 10.1016/j.epsl.2007.01.001.

Collettini C., Holdsworth R.E., Smith S.A.F. 2009. Fault Zone Structure and Deformation Processes along an Exhumed Low-Angle Normal Fault: Implications for Seismic Behaviour Review Article. *International Geophysics*, **94**, 69-85

Cowan, D.S., 1999, Do faults preserve a record of seismic slip? A field geologist's opinion: *Journal of Structural Geology*, **21**, 995-1001.

Cox, S.F. 1987. Antitaxial crack-seal vein microstructures and their relationship to displacement paths. *Journal of Structural Geology*, **9**, 779-787.

Cox, S.F. 2010. The application of failure mode diagrams for exploring the roles of fluid pressure and stress states in controlling styles of fracture-controlled permeability enhancement in faults and shear zones. *Geofluids*, **10,** 217–233, doi: 10.1111/j.1468-8123.2010.00281.x

Deer, W.A., Howie, R.A., Zussman, J., 1992. *An Introduction to the Rock-Forming Minerals*. Longman, Harlow.

Deichmann, N., D. Giardini, 2009, Earthquakes Inducedby the Stimulation of an Enhanced Geothermal System below Basel, Switzerland, *Seismological Research. Letters*, **80**, 784-798.

Del Moro A., Pardini, G. Quercioli, C., Villa, I.M., Callegari, E. 1983. *Rb/Sr and K/Ar chronology of Adamello granitois, Southern Alps***.** Memoir Società Geologica Italiana, **26,** 285–299

Delvaux, D., Sperner B., 2003. New aspects of tectonic stress inversion with reference to the TENSOR program. *In:* D.A. Nieuwland (ed.), *New Insights into Structural Interpretation and Modelling*, Geological Society, London, Special Publications, **212,** 75-100.

Di Toro, G., Pennacchioni, G., 2004. Superheated friction-induced melts in zoned pseudotachylytes within the Adamello tonalites (Italian Southern Alps). *Journal of Structural Geology*, **26,** 1783-1801.

Di Toro, G., Pennacchioni, G., 2005. Fault plane processes and mesoscopic structure of a strong-type seismogenic fault in tonalites (Adamello batholith, Southern Alps). *Tectonophysics*, **402**, 54-79

Etchecopar, A., Vasseur, G., Daignières, M., 1981. An inverse problem in microtectonics for the determination of stress tensors from fault striation analyses. *Journal of Structural Geology*, **31,** 51–65.

Ferrill, D.A., Winterle, J., Wittmeyer, G., Sims, D., Colton, S., Argmstrong, A., Morris, A.P., 1999. Stressed rock strains groundwater at Yucca Mountain, Nevada. *GSA Today*, 9, 1–8.

Fischer, T., Horálek J., Hrubcová, P., Vavryčuk, V., Bräuer, K., Kämpf, H. 2013. Intra-continental earthquake swarms in West-Bohemia and Vogtland: A review. *Tectonophysics*, http://dx.doi.org/10.1016/j.tecto.2013.11.001

Hansmann A. W., Oberli, F. 1991. Zircon inheritance in an igneous rock suite from the southern Adamello batholith (Italian Alps). *Contributions to Mineralogy and Petrology*, **107,** 501–518.

Godano, M., Larroque, C., Bertrand, E., Courboulex, F., Deschamps,A., Salichon,J., Blaud-Guerry, C., Fourteau, L., Charléty, J. Deshayes,P. 2013. The October–November 2010 earthquake swarm near Sampeyre (Piedmont region, Italy): A complex multicluster sequence, *Tectonophysics*, **608,** 97-111, dx.doi.org/10.1016/j.tecto.2013.10.010.

Hilgers C., Urai J. L. 2005. On the arrangement of solid inclusions in fibrous veins and the role of the crack-seal mechanism. *Journal of Structural Geology*, **27**, 481-494.

Jaeger J.C., Cook N.G.W., Zimmerman R.W. 2007. *Fundamentals of Rock Mechanics* (4th edition) Blackwell Publishing, pp 475.

763 Kassaras, I., Kapetanidis, V., Karakonstantis, A., Kouskouna, V., Ganas, A., Chouliaras, G.
764 Drakatos G., Moshou, A., Mitropoulou, V., Argyrakis, P., Lekkas, E., Makropoulos, K. 2014.
765 Constraints on the dynamics and spatio-temporal evolution of the 2011 Oichalia seismic
766 swarm (SW Peloponnesus, Greece) *Tectonophysics*, 614, 100–127; doi:
767 10.1016/j.tecto.2013.12.012
768
769 King, G.C.P., Stein, R.S., Lin, J., 1994. Static stress changes and the triggering of
770 earthquakes, *Bulletin of the Seismological Society of America*, **84**, 935-953.
771
772 Kirkpatrick, J. D., Z. K. Shipton, J. P. Evans, S. Micklethwaite, S. J. Lim, and P. McKillop
773 2008, Strike-slip fault terminations at seismogenic depths: The structure and kinematics of
774 the Glacier Lakes fault, Sierra Nevada United States, *Journal of Geophysical Research,* **113**,
775 B04304, doi:10.1029/2007JB005311.
776
777 Kisslinger, C., 1975. Processes during the Matsushiro swarm as revealed by levelling,
778 gravity, and spring-flow observations, *Geology*, **3,** 57–62.
779
780 Lin, J., and Stein, R.S., 2004, Stress triggering in thrust and subduction earthquakes, and
781 stress interaction between the southern San Andreas and nearby thrust and strike-slip faults:
782 *Journal of Geophysical Reearch,* 109, B02303, doi:10.1029/2003JB002607.
783
784 Lisle, R.J., and Srivastava, D.C., 2004, Test of the frictional reactivation theory for faults and
785 validity of fault-slip analysis: *Geology*, **32**, 569-72.
786
787 Main, I.G., 1996. Statistical physics, seismogenesis, and seismic hazard. *Reviews of*
788 *Geophysics*, 34, 433–462.
789
790 Mayer A., Cortiana, G., Dal Piaz, G.V., Deloule, E., De Pieri, R., Jobstraibizer, P. 2003. U–
791 Pb single zircon ages of the Adamello batholith, Southern Alps. *Memoir Società Geologica*
792 *Italiana*, **55,** 151–167.
793
794 Michael, A.J., 1984. Determination of stress from slip data: faults and folds. *Journal of*
795 *Geophysical Research,* 89, 11517-11526.
796

Micklethwaite, S., Cox, S. F. 2004. Fault-segment rupture, aftershock-zone fluid flow, and mineralization. *Geology*, **32,** 813-816.

Miller S. A., Collettini C., Chiaraluce L., Cocco M., Barchi M. & Kaus B. J. P. 2004. Aftershocks driven by a high pressure CO2 source at depth. *Nature*, **427**,724-727.

Mittempergher, S., Pennacchioni,G., Di Toro, G. 2009. The effects of fault orientation and fluid infiltration on fault rock assemblages at seismogenic depths. *Journal of Structural Geology,* **31,** 1511-1524.

Mittempergher, S., Dallai, L. Pennachioni, G., Renard, F., Di Toro, G. 2014. Origin of hydrous fluids at seismogenic depth: constraints from natural and experimental fault rocks, *Earth and Planetary Science Letters*, **385,** 97-109.

Mogi K. 1963. Some discussions of aftershocks, foreshocks and earthquakes swarms –the fracture of a semi-infinite body caused by an inner stress origin and its relation to earthquake phenomena. *Bulletin of the Earthquake Research Institute*, **41**, 615–658.

Morris, A.P., Ferrill, D.A., Henderson, D.B., 1996. Slip tendency and fault reactivation. *Geology*, **24**, 275–278.

Mueller K, Hough S. E., Bilham R., 2004. Analysing the 1811–1812 New Madrid earthquakes with recent instrumentally recorded aftershocks. *Nature*, **429**, 284-288.

Niemeijer, A., Di Toro, G., Griffith, W.A., Bistacchi, A., Smith, S. a. F., Nielsen, S., 2012. Inferring earthquake physics and chemistry using an integrated field and laboratory approach. *Journal of Structural Geology,* **39,** 2–36.

Noir, J., Jacques, E., Bekri, S., Adler, P.M., Tapponnier, P. & King, G.C.P., 1997. Fluid flow triggered migration of events in the 1989 Dobi earthquake sequence of Central Afar, *Geophysics Research Letters,* **24,** 2335–2338.

Nur, A., Booker, J.R., 1972. Aftershocks caused by pore fluid flow? *Science,* **175,** 885-887.

831 Nur, A., Byerlee, J.D. 1971. An exact effective stress law for elastic deformation of rock with
832 fluids. *Journal of Geophysical Research,* **76,** 6414-6419.
833
834 Pennacchioni G., Di Toro, G.. Brack, P., Menegon, L., Villa, I.M. 2006. Brittle–ductile–
835 brittle deformation during cooling of tonalite (Adamello, Southern Italian Alps),
836 *Tectonophysics*, **427**, 171-197
837
838 Phillips, W.J. 1972. Hydraulic fracturing and mineralisation. *Journal of the Geological*
839 *Society of London*, **128,** 337-359.
840
841 Prosser, G. 1998. Strike-slip movements and thrusting along a transpressive fault zone: The
842 North Giudicarie line (Insubric line, northern Italy). *Tectonics*, **17**, 921–937.
843
844 Raleigh, C.B., Healy, J.H, Bredehoeft,J.D. 1976, An Experiment in Earthquake Control at
845 Rangely, Colorado, *Science*, **191**, 1230-1237.
846
847 Reasenberg, P.A., Simpson, R.W. 1992. Response of regional seismicity to the static stress
848 change produced by the Loma Prieta earthquake. *Science,* **255,** 1687-1690.
849
850 Reches, Z., 1987. Determination of the tectonic stress tensor from slip along faults that obey
851 the Coulomb yield condition. *Tectonics*, **6,** 849–861.
852
853 Reverman R.L., Fellin M.G., Herman F., Willett S.D., Fitoussi C., 2012. Climatically versus
854 tectonically forced erosion in the Alps: Thermochronometric constraints from the Adamello
855 Complex, Southern Alps, Italy. *Earth and Planetary Science Letters*, **339,** 127-138.
856
857 Rowe, C. D., Kirkpatrick, J. D. and Brodsky, E. E. 2012. Fault rock injections record paleo-
858 earthquakes. *Earth and Planetary Science Letters*, **335-336**, 154-166.
859
860 Scholz C.H. 2002. *The Mechanics of Earthquakes and Faulting*. Cambridge University Press,
861 New York, pp 439.
862

Seeber, L., Armbruster, J.G. and Kim,Y.K. 2004. A Fluid-Injection Earthquake Sequence in Ashtabula, Ohio: Implications for Seismogenesis in Stable Continental Regions, *Bulletin of the Seismological Society of America,* **94**, 76-87.

Shapiro, S.A., Rentsch, S., Rothert, E., 2005. Characterization of hydraulic properties of rocks using probability of fluid-induced microearthquakes. *Geophysics,* **70,** F27-F33.

Shearer, P.M., Hardebeck, J.L., Astiz, L., Richards-Dinger, K.B. 2003. Analysis of similar event clusters in aftershocks of the 1994 Northridge, California, Earthquake. *Journal of Geophysical Research,* 108 (B1) 2035, doi: 10.1029/2001JB000685.

Shumway A. M., 2008. Focal Mechanisms in the Northeast New Madrid Seismic Zone. *Seismological Research Letters.* **79**, 469-477.

Sibson, R.H. 1981. Fluid flow accompanying faulting: field evidence and models. In: Simpson, D .W., Richards, P.G., (eds.). *Earthquake Prediction: an International Review.* Maurice Ewing Series 4, American Geophysical Union, Washington D.C., 593-603.

Sibson R.H. 1985a, Stopping of earthquake ruptures at dilational fault jogs: *Nature,* **316,** 248-251.

Sibson, R.H., 1985b. A note on fault reactivation. *Journal of Structural Geology,* **7,** 751-754.

Sibson, R. H. 1993. Load-strengthening versus load-weakening faulting. *Journal of Structural Geology,* **15,** 123-128.

Sibson, R. H. 1995. Structural permeability and fluid flow in fault-fracture meshes. In: Mauk, J. L., St George, J. D. (eds). *Proceedings of the 1995 PACRIM Congress, Auckland, New Zealand, 19-22 November 1995.* The Australasian Institute of Mining and Metallurgy Publication Series **9/95**, 521-526.

Sibson R.H., Robert F., Poulsen K.H. 1988. High-angle reverse faults, fluid-pressure cycling and mesothermal gold-quartz deposits. *Geology,* **16**, 551–55.

Sleep, N. H., Blanpied, M. L., 1992, Creep, compaction and the weak rheology of major faults, *Nature,* **359,** 687-692.

Smith S.A.F., Collettini C., Holdsworth R.E. 2008. Recognizing the seismic cycle along ancient faults: CO2-induced fluidization of breccias in the footwall of a sealing low-angle normal fault. *Journal of Structural Geology,* **30,** 1034-1046.

Smith, S.A.F., Bistacchi, A., Mitchell, T., Mittempergher, S., DiToro, G., 2013. The structure of an intraplate exhumed seismogenic fault in crystalline basement. *Tectonophysics,* **599,** 29–44.

Stein R.S. Barka A.A. Dieterich, J.H. 1997. Progressive failure on the North Anatolian fault since 1939 by earthquake stress triggering. *Geophysical Journal International,* **128:** 594-604.

Stipp M., B. Fügenschuh, L.P. Gromet, H. Stünitz & S.M. Schmid, 2004. Contemporaneous plutonism & strike-slip faulting: a case study from the Tonale fault zone north of the Adamello pluton (Italian Alps). *Tectonics*, **23**, p. TC3004.

Sykes, L. R. 1978. Intraplate seismicity, reactivation of preexisting zones of weakness, alkaline magmatism and other tectonism postdating continental fragmentation. *Reviews of Geophysics and Space Physics*, **16,** 621-88.

Toda, S., Stein, R.S., Richards-Dinger, K., and Bozkurt, S., 2005, Forecasting the evolution of seismicity in southern California—animations built on earthquake stress transfer: *Journal of Geophysical Research,* 110, B05S16, doi:10.1029/2004JB003415.

Townend, J., and Zoback, M.D. 2000. How faulting keeps the crust strong, *Geology*, **28,** 399-402.

Twiss R. J., Moores E. M. 1992. *Structural Geology*. W.H. Freeman & Company, pp.

927 Viola G., N.S. Mancktelow & D. Seward. 2001. Late Oligocene–Neogene evolution of
928 Europe–Adria collision: new structural & geochronological evidence from the Giudicarie
929 fault system (Italian Eastern Alps). *Tectonics*, **20**, 999–1020.
930
931 Wallace, R.E., 1951. Geometry of shearing stress and relation to faulting. *Journal of*
932 *Geology,* **59**, 118–130.
933
934 Walker, R.J., Holdsworth, R.E., Armitage, P.J., Faulkner, D.R., 2013a. Fault zone
935 permeability structure evolution in basalts, *Geology*, **41**, 59-62.
936
937 Walker, R.J., Holdsworth, R.E., Imber, J., Faulkner, D.R., Armitage, P.J., 2013b. Fault zone
938 architecture and fluid flow in interlayered basaltic volcaniclastic-crystalline sequences,
939 *Journal of Structural Geology*, **51**, 92–104.
940
941 Wibberley, C.A.J.,2002. Hydraulic diffusivity of fault gouges and implications for thermal
942 pressurization during seismic slip. *Earth, Planets Space*, **54**, 1153-1171.
943
944 Weisenberger, T., Bucher, K. 2010. Zeolites in fissures of granites and gneisses of the Central
945 Alps. *Journal of Metamorphic Geology*, **28,** 825-847.
946
947 Weisenberger T.B., Rahn M. van der Lelji R., Spikings R. & Bucher K. 2012. Timing of
948 low-temperature mineral formation during exhumation and cooling in the Central Alps,
949 Switzerland. *Earth and Planetary Science Letters*. 327-328, 1-8, doi:
950 10.1016/j.epsl.2012.01.007.
951
952 Wells, D.L., Coppersmith, K.J., 1994. New Empirical Relationships among Magnitude,
953 Rupture Length, Rupture Width, Rupture Area, and Surface Displacement. *Bulletin of the*
954 *Seismological Society of America,* **84,** 974–1002.
955
956 Yamaji, A., 2000. The multiple inverse method: a new technique to separate stresses from
957 heterogeneous fault-slip data. *Journal of Structural Geology*, **22,** 441–452.
958
959 Yardley, B.W.D. 1997. The evolution of fluids through the metamorphic cycle. In: Jamtveit,
960 B. & Yardley, B.W.D. (eds) *Fluid Flow and Transport in Rocks.* Chapman & Hall, 99-117.

Zoback M.D. Reservoir Mechanics (2007) Cambridge University Press, pp.449.

Table Caption

Table 1: XRD analyses from zeolite mineralized veins in the Lobbia Glacier Valley area. For further details see Appendix 1.

Figure Captions

Figure 1. (a) Schematic geological map of the Adamello region. GLFZ = Gole Larghe Fault Zone; PCFZ = Passo Cercen Fault Zone; LF = Lares Fault. Red box shows location of study area. (b) Aerial photograph of the study area with numbered faults (NNE-SSW sinistral = green (S); E-W sinistral-reverse = red (T); N-S normal = blue (N)). Black dashed contact and yellow shaded zone are, respectively, the southern margin of the GLFZ and central zone of K-feldspar-epidote-chlorite alteration according to Smith et al. (2013). Box shows location of Figure 4. (c) An oblique aerial view looking S showing the typical appearance of the fractured tonalities in the glacier valley. The largest fault, S1, lies in the centre of the valley.

Figure 2. Examples of fractures and zeolite mineralization. (a) Altered damage zone and vein fracture meshes along fault N1. Oblique cross-section view. (b) Plan view of composite tensile vein related to fault N3 with multi-coloured zeolite fills. Arrows show offset trajectories (c) From E to W, wall rock, altered damage zone and core with red gouge in cross-section view of sinistral fault S2. Note steep mylonitic foliation in both wall rock and damage zone indicative of reactivation of a pre-existing sinistral shear zone.(d) Cross-sectional view of linked fractures and altered damage zone along sinistral-reverse thrust fault T1. Note linking sub-horizontal R-shears. Box shows location of Fig 3d. (e) Down-slope view of prominent gulley feature following sinistral fault S3. Valley sides are defined by two NNE-SSW sinistral faults (green) while the central region and wall rocks are cut by en-echelon sets of N-S normal faults (blue). (f) Oblique section view of interlinked and cross-cutting fracture sets (labelled) developed in the upper part of the GLFZ. Note the <2m sinistral offset of fault T1 by S1 and the linkage of faults T1 and N3. The gouge injections shown in Fig 6a occur at the latter junction.

Figure 3. Fracture kinematics, linkage and zeolite mineralization. (a) Shallowly-plunging slickenlines (arrows) within zeolite-bearing gouge on a NNE-SSW sinistral fault related to fault S3. Note earlier pale zeolite tensile fracture fill at the margins of the fault. (b) Plan-view of zeolite-bearing composite fault zone related to fault S1 with breccia and gouge showing prominent development of T-fractures consistent with sinistral shear. Note alteration halo in wall rocks adjacent to fault. (c) View of steeply plunging slickenlines along zeolite vein filling N-S normal fault associated with fault N3. (d) Close-up section view of SSW-dipping slip surface in fault T1 with cm-scale, top-to-the-left offsets of the pale aplite vein along sub-horizontal linking R-fractures in the fault hangingwall. Also shows orange-brown zeolite gouges developed along the underlying slip surface and the pre-existing protomylonitic foliation reactivated by the E-W fault zone. (e) Plan view of linked NNE-SSW sinistral faults and N-S normal/tensile fractures (arrows). (f) Oblique view of slip surface showing

overprinting dip-slip and later (sinistral) strike-slip slickenlines. Note that the fracture surface changes strike from N-S (right) to NNE-SSW (left) possibly marking the linkage of a N-S normal and NNE-SSW sinistral segment.

Figure 4. Detailed map of the zeolite-bearing fracture patterns around fault S1 (see Fig. 1b). The density of fractures moving away from the main fault decreases, as do the fault damage zone thicknesses along the linking E-W sinistral reverse faults.

Figure 5. Evidence for multiple slip-mineralization events. (a) Plan view of sheared and cataclastically deformed composite zeolite vein associated with fault N3. (b) Mineralized zeolite gouge with angular fragments of wall rocks and earlier pale zeolite veins. Plan view of fault N2.

Figure 6. Zeolite-mineralized gouge injections. (a) Section view of gouge-filled N-S tensile fractures (arrowed) developed in footwall of the sinistral-reverse fault T1. Note that the T1 slip surface is filled with the same gouge. (b) Sectional view of N-S tensile fractures filled with a least 2 phases of injected zeolite gouge (early pale coarser phase and later dark, finer phase). Located in the footwall of fault T3. (c) Sectional view of orange-red zeolite gouge-breccia with earlier zeolite, epidote cataclasite and granite clasts close to fault T3. (d) Section cut through a sample of the E-W zeolite T1 fault gouge shown in (a) highlighting multiple generations of gouge and injection events. The section is cut parallel to transport and the obliquity of the injections is consistent with the inferred sinistral-reverse shear sense.

Figure 7. Microstructural development of zeolite mineralisation. All images are in cross-polars. (a) Zoned zeolite vein showing anhedral crystals towards the vein wall, acicular needles, and fine-grained acicular needles towards the centre of the vein. (b) Later shearing leading to cataclasis and the formation of suspended clasts of vein material. (c) Homogeneous zeolite cataclasite. (d) Crystalline haloed clasts of zeolite cataclasite suspended in a fine-grained zeolite gouge. (e) Tensile fracturing of a gouge (with haloed zeolite cataclasite clasts) forming a new zeolite vein at the right-hand margin. (f) Injection of fine grained zeolite gouge (highlighted by dashed lines) through a zeolite vein & cataclasite. (g) Repeated crack seal textures in a zeolite vein.

Figure 8. Equal area stereoplots of pre-existing structures (cooling joints, aplite sheets, shear zone mylonites and cataclasites-pseudotachylytes) compared to the stereoplots showing the various zeolite-bearing fractures. The close similarities in orientation are consistent with the reactivation of the variously oriented pre-existing structures observed in the field. The structures are ordered in terms of their relative age and depth of formation, with those on the left forming first and at greatest depths (see Pennacchioni et al., 2006).

Figure 9. Left and centre: kinematic data and paleostress inversion results for all zeolite-bearing brittle faults in the Lobbia Glacier valley. Right: Mohr plot representing the reduced (adimensional) deviatoric stress tensor (axes are in percent of σ_1); See Delvaux and Sperner (2003) for details. The calculated stress states for the NNE-SSW sinistral, N-S normal (both black) and E-W sinistral-reverse (red) faults are also shown.

Figure 10. Stereographic (left) and Mohr plots (right) of Normalized Slip Tendency (NST; top) and Dilation Tendency (DT; bottom). Red = high NST or DT; blue = low NST or DT;

pale blue dots = Andersonian orientations; white polygons = principal stress axes; white dots = poles to main fault sets.

Figure 11. (a) Coulomb stress model M3 rupture events along NNE-SSW sinistral fault S1 showing stress loading magnitudes (red = increase in Coulomb stress; blue = decrease in Coulomb stress) and local transient reorientations of horizontal displacement directions (arrows). (b) Basic fault map highlighting regions which have become more likely to fail because of the stress transfer associated with the rupture of S1. (c) Stereographic projection showing the rake of lineation (red dot) on the E-W sinistral-reverse faults predicted by the modelling in (a), compared to the lineations observed in the field (black dots). (d) 3D block diagram looking south showing the geometric relationships between the reactivation of pre-existing structures following stress transfer onto E-W faults.

Figure 12. Graph showing the characteristic timescales (τ) for diffusion across a range of distances (500 to 10000 m). Hydraulic diffusivities (κ) are taken directly from: (a) estimates of the *in situ* macroscopic fluid diffusion tensor beneath the Afar rift (Noir *et al*., 1997); and (e) *in situ* studies of fluid injection into geothermal reservoirs (Shapiro *et al*., 2003), or derived from permeability values obtained from (b) modelling the aftershock propagation velocity following the Umbria-Marche earthquakes (M_w = 5.7, 6) (Miller *et al*., 2004); (c and d) static measurements on small, zeolite- and calcite-bearing faults under a range of confining pressures (Walker *et al*., 2013a, b); and (f) estimates for intraplate continental crust (Townend and Zoback, 2000). (b), (c), (d) and (f) assume porosity (ϕ) = 0.02), fluid compressibility (β_f) = $5\text{x}10^{-10}$ Pa^{-1}, rock compressibility (β_r) = $2\text{x}10^{-11}$ Pa^{-1}, and fluid viscosity (η) = $1.9\text{x}10^{-4}$ Pas (Townend and Zoback, 2000).

Figure 13. Cartoon showing the proposed rupture-reactivation-cementation cycle. Initially (i) deep seated tectonically-induced rupture allows (ii) fluids to enter the system. At this stage pre-existing structures are stable, but increasing stress and/or pore fluid pressure associated with rupturing along fault S1 eventually leads to other NNE-SSW and N-S orientated pre-existing structures being reactivated. Mineralisation of the fractures occurs (iii) as fluid pressures fall, leading to cementation and sealing. This reduces permeability allowing the re-establishment of high pore fluid pressures, restarting the rupture-reactivation-cementation cycle (iv-vi, vii-ix, etc).The mainshocks (bigger) and aftershock (smaller) focal mechanisms shown are purely schematic with kinematics based on outcrop patterns and stress inversions.

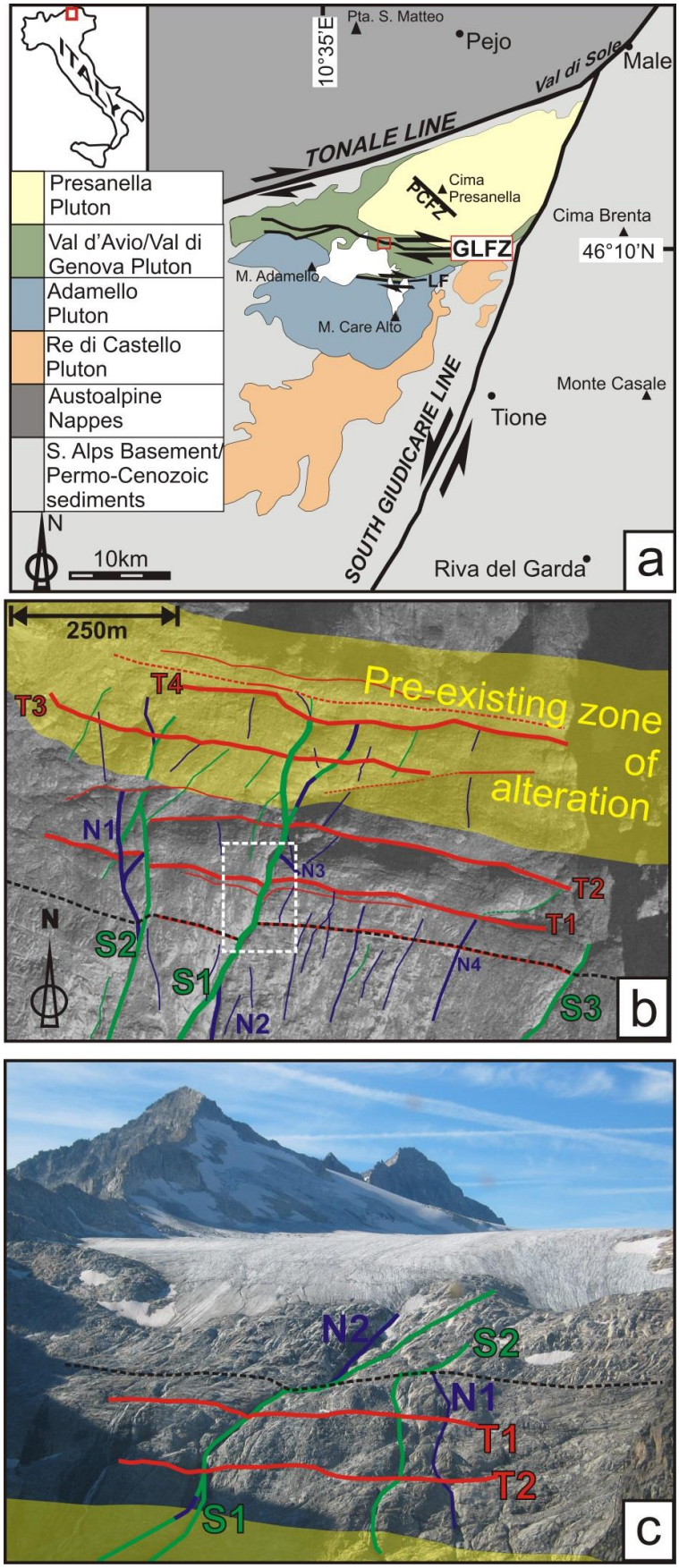
Pta. S. Matteo
10°35'E
Pejo
Male
Val di Sole
TONALE LINE
PCFZ
Cima Presanella
Cima Brenta
GLFZ
46°10'N
M. Adamello
LF
M. Care Alto
Monte Casale
Tione
SOUTH GIUDICARIE LINE
Riva del Garda
Presanella Pluton
Val d'Avio/Val di Genova Pluton
Adamello Pluton
Re di Castello Pluton
Austoalpine Nappes
S. Alps Basement/ Permo-Cenozoic sediments
N
10km
a
250m
T4
T3
Pre-existing zone of alteration
N1
N3
T2
T1
N
S2
S1
N2
N4
S3
b
N2
S2
N1
T1
T2
S1
c

Fig 1

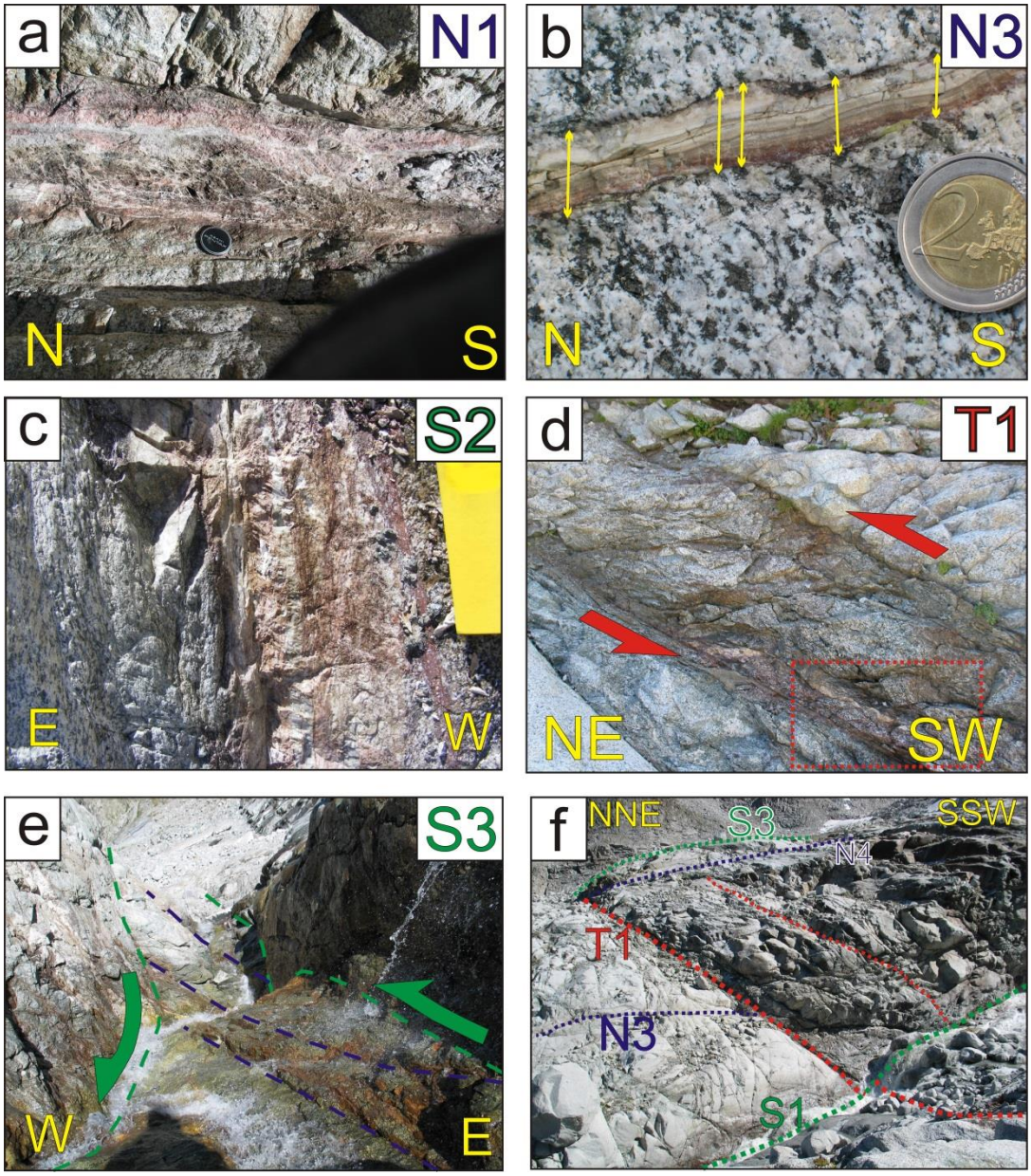

Fig 2

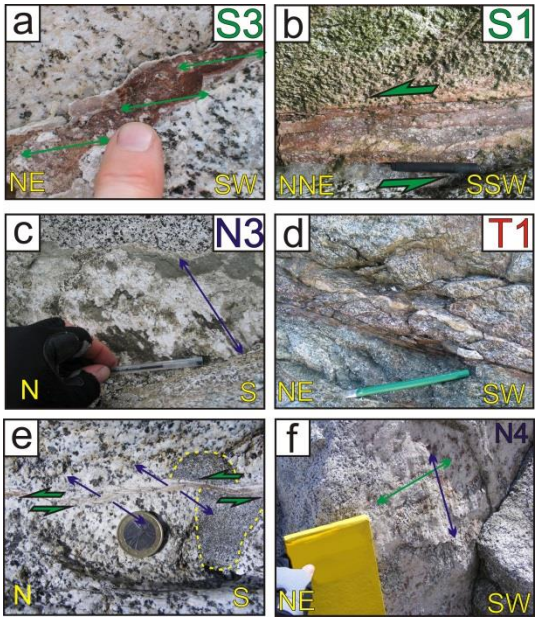

Fig 3

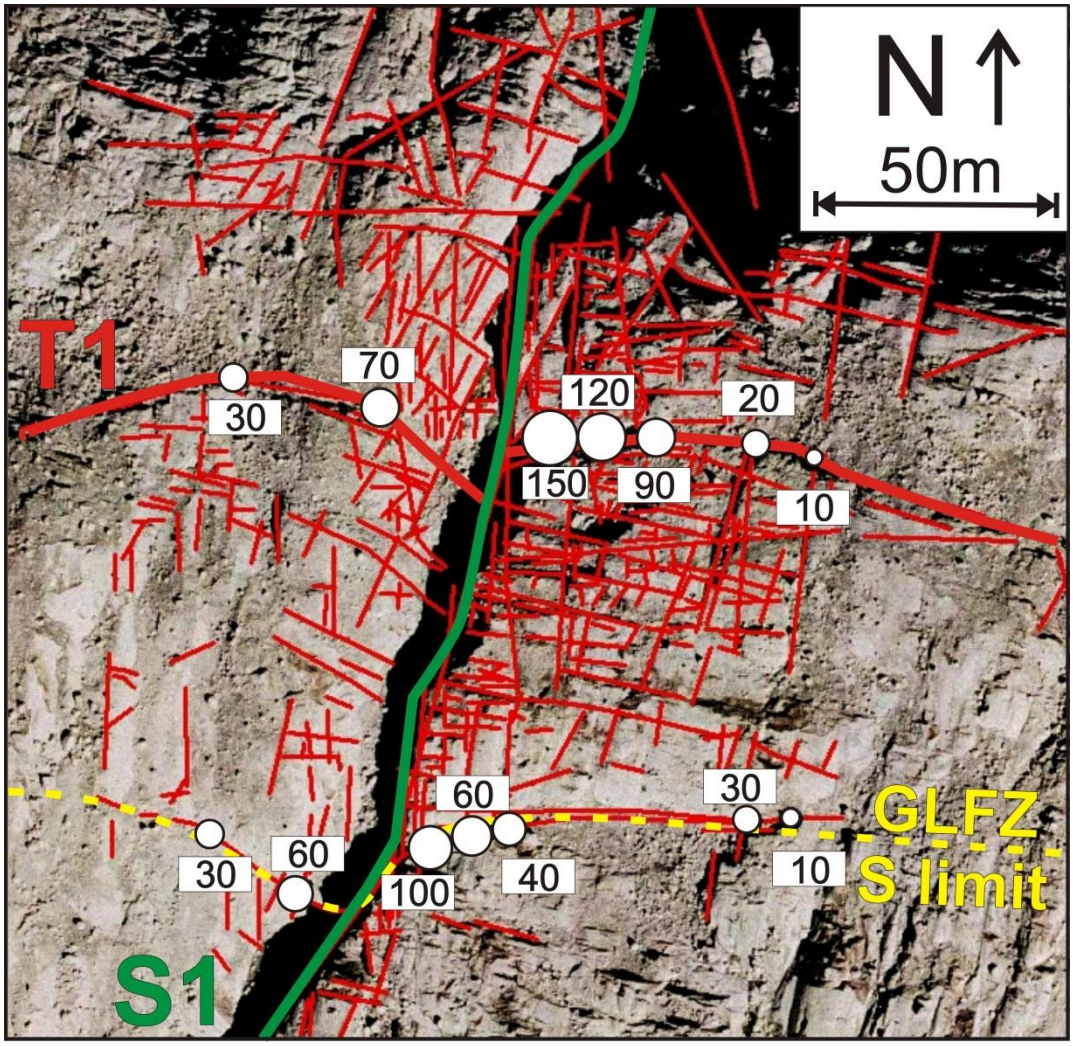

Fig 4

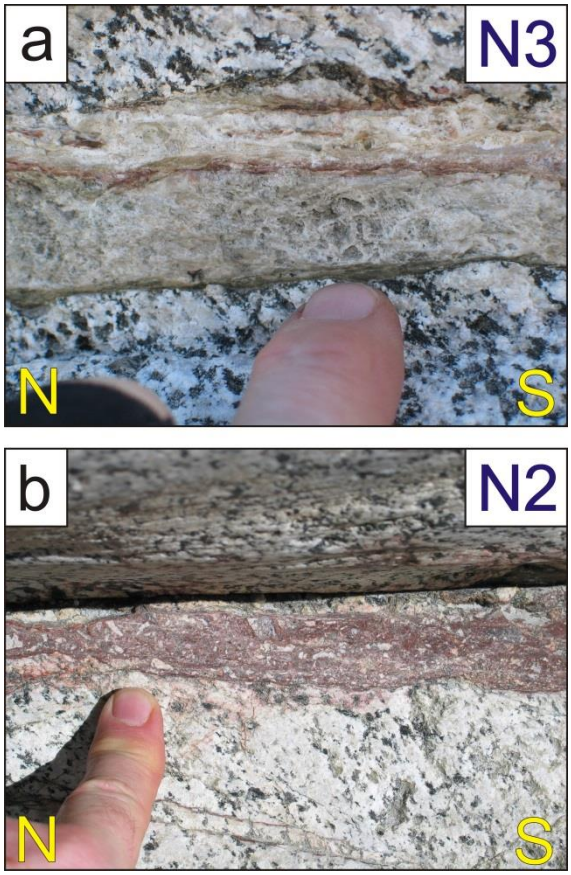

Fig 5

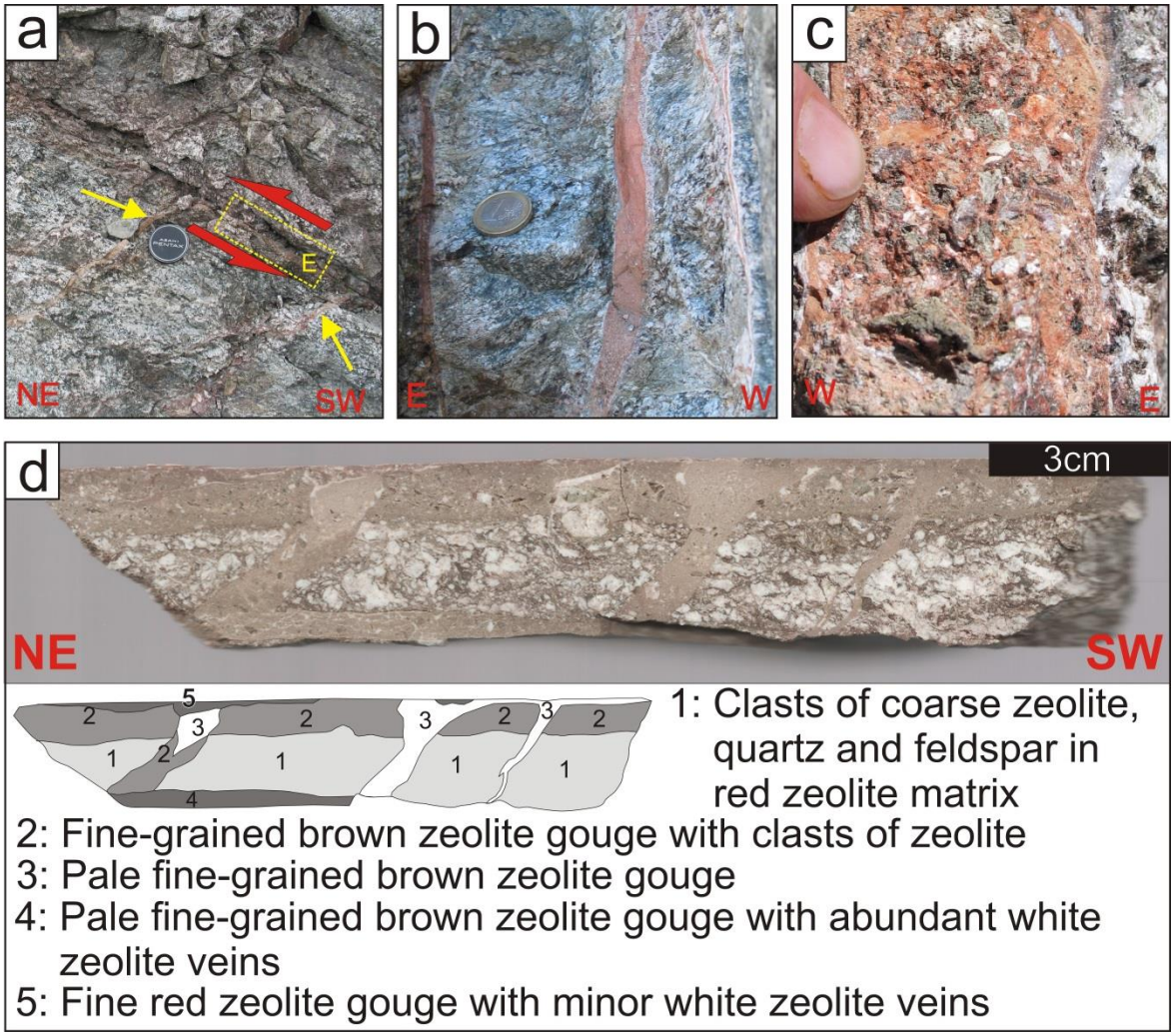
a
NE
SW
E
b
E
W
c
W
E
d
3cm
NE
SW
5
2
3
2
3
2
3
2
1
2
1
1
1
4
1: Clasts of coarse zeolite, quartz and feldspar in red zeolite matrix
2: Fine-grained brown zeolite gouge with clasts of zeolite
3: Pale fine-grained brown zeolite gouge
4: Pale fine-grained brown zeolite gouge with abundant white zeolite veins
5: Fine red zeolite gouge with minor white zeolite veins

Fig 6

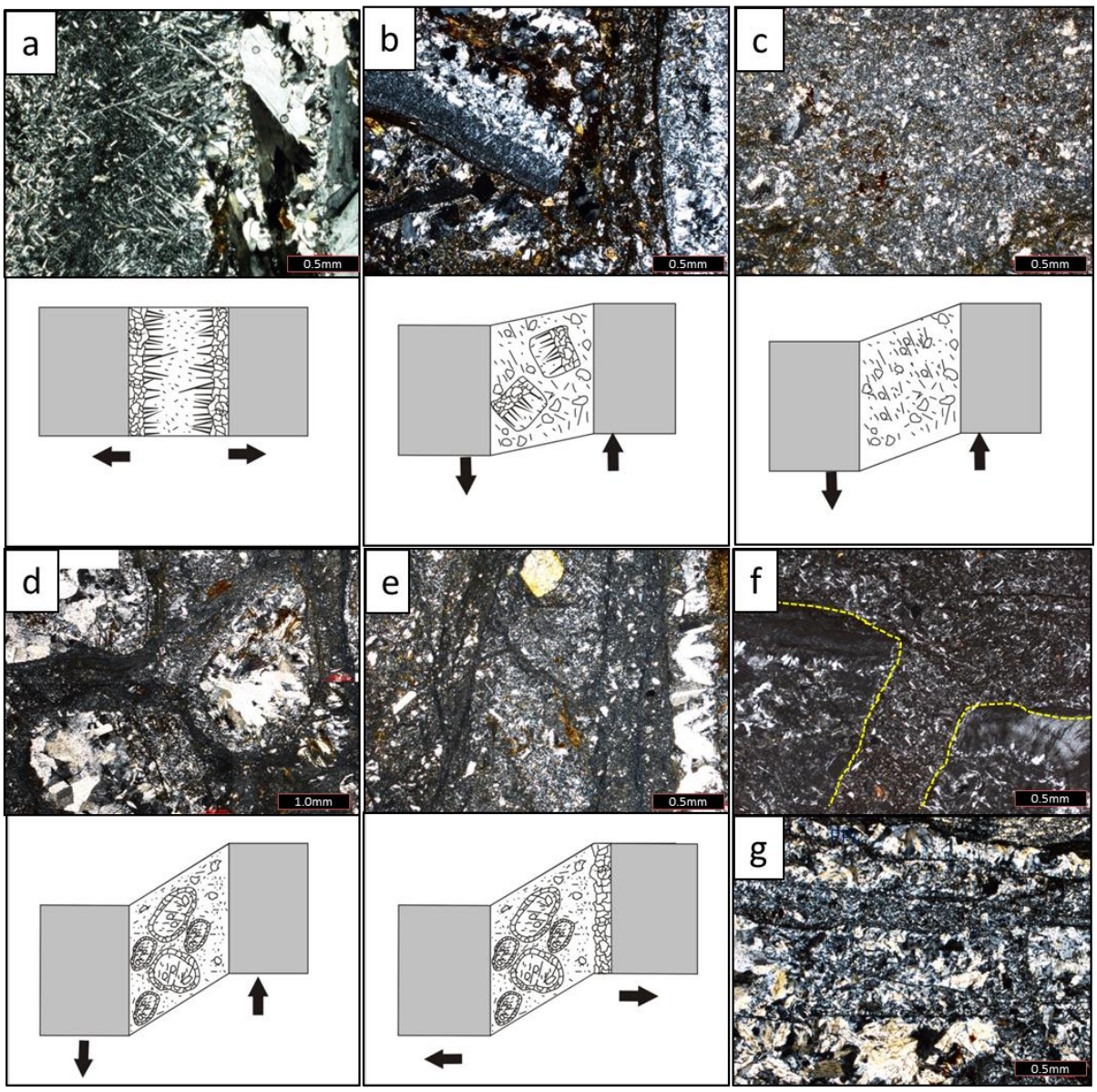

Fig 7

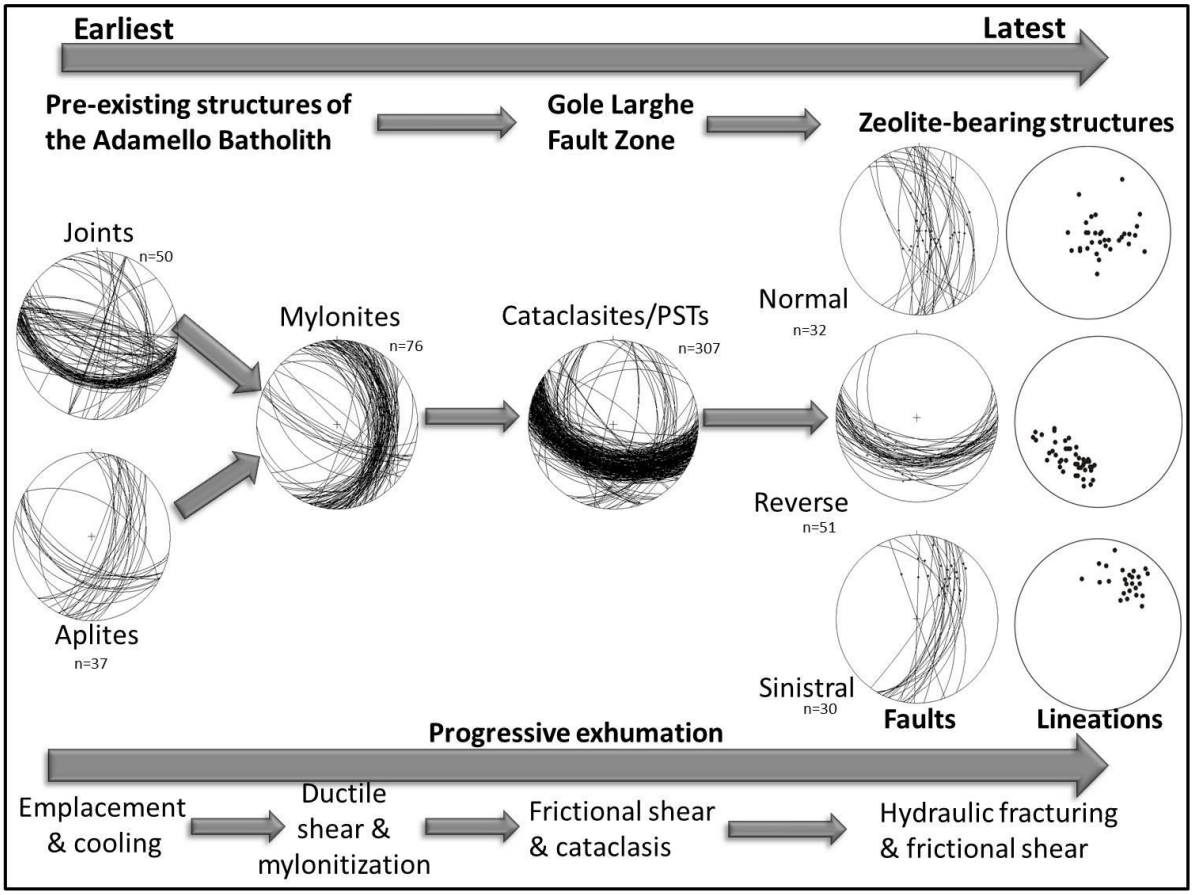
Earliest
Latest
Pre-existing structures of the Adamello Batholith
Gole Larghe Fault Zone
Zeolite-bearing structures
Joints
n=50
Mylonites
n=76
Cataclasites/PSTs
n=307
Normal
n=32
Reverse
n=51
Sinistral
n=30
Aplites
n=37
Faults
Lineations
Progressive exhumation
Emplacement & cooling
Ductile shear & mylonitization
Frictional shear & cataclasis
Hydraulic fracturing & frictional shear

Fig 8

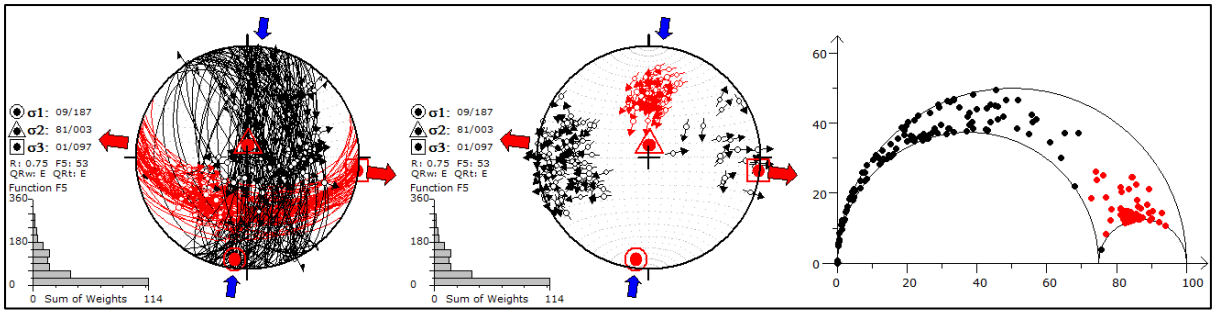
σ1: 09/187
σ2: 81/003
σ3: 01/097
R: 0.75 F5: 53
QRw: E QRt: E
Function F5
360
180
0
0 Sum of Weights 114
σ1: 09/187
σ2: 81/003
σ3: 01/097
R: 0.75 F5: 53
QRw: E QRt: E
Function F5
360
180
0
0 Sum of Weights 114
60
40
20
0
0 20 40 60 80 100

Fig 9

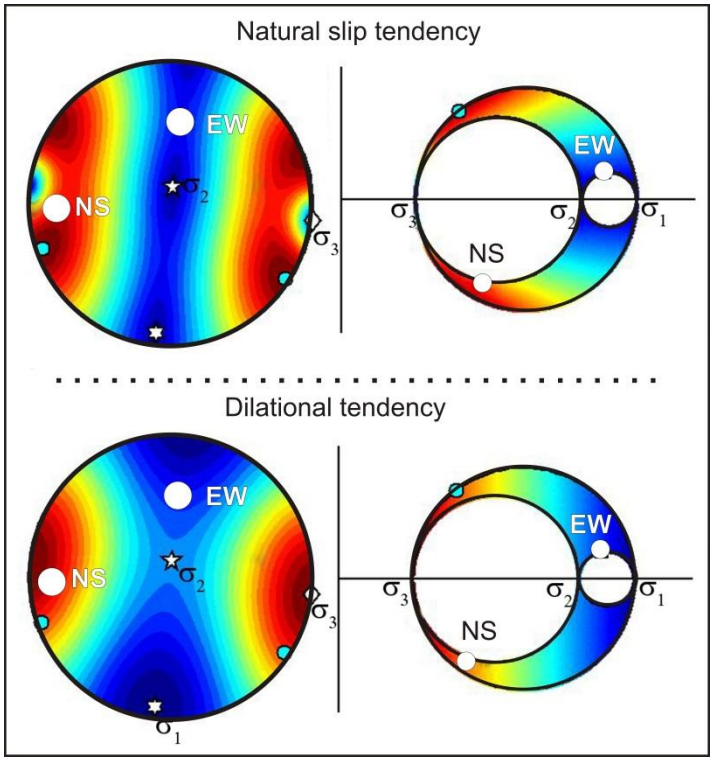
Natural slip tendency
EW
NS
σ2
σ3
EW
σ3
σ2
σ1
NS
Dilational tendency
EW
NS
σ2
σ3
EW
σ3
σ2
σ1
NS
σ1

Fig 10

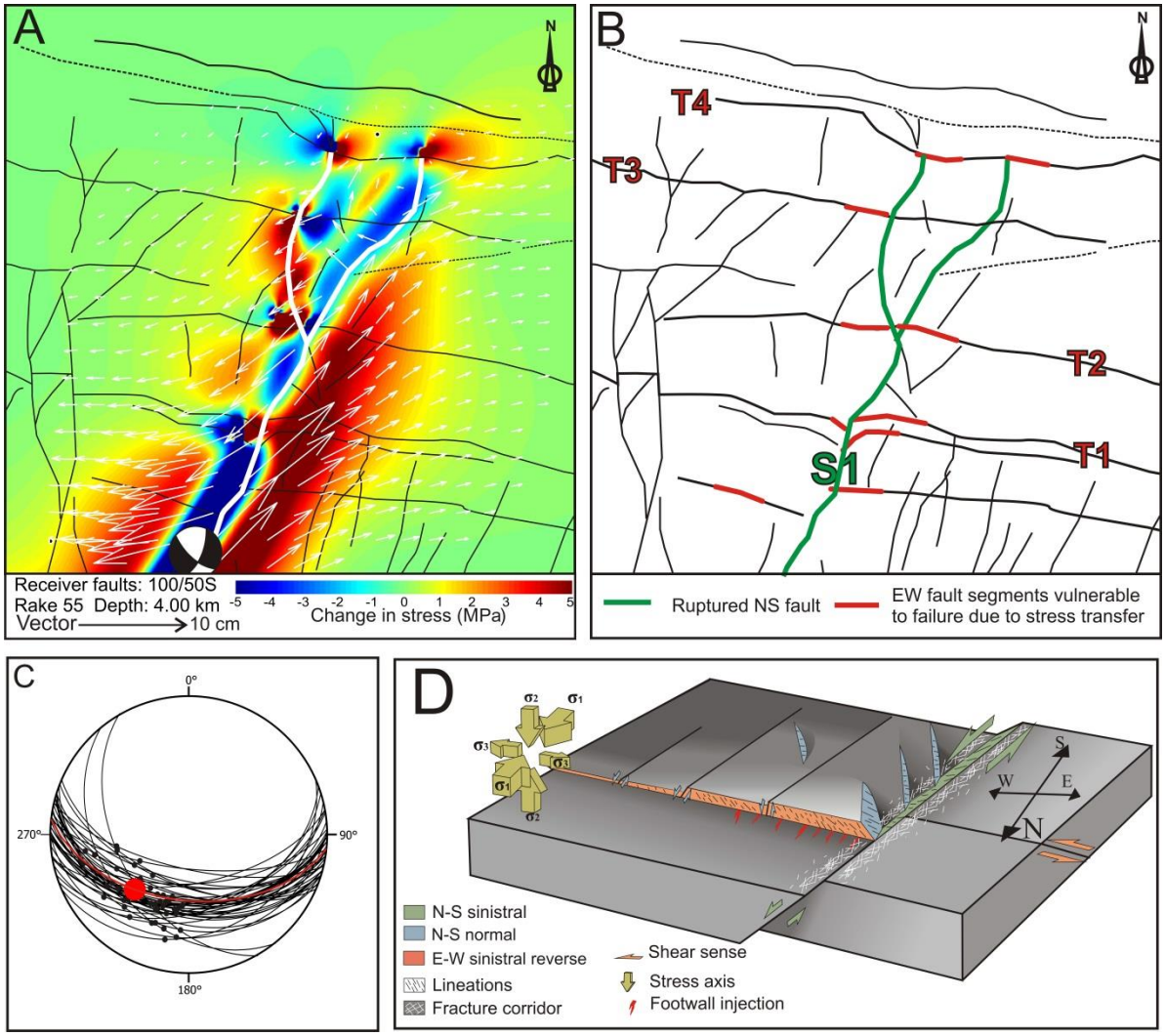
A
N
Receiver faults: 100/50S
Rake 55 Depth: 4.00 km
Vector 10 cm
-5 -4 -3 -2 -1 0 1 2 3 4 5
Change in stress (MPa)
B
N
T4
T3
T2
T1
S1
Ruptured NS fault
EW fault segments vulnerable to failure due to stress transfer
C
0°
270°
90°
180°
D
σ2
σ1
σ3
σ3
σ1
σ2
S
W
E
N
N-S sinistral
N-S normal
E-W sinistral reverse
Lineations
Fracture corridor
Shear sense
Stress axis
Footwall injection

Fig 11

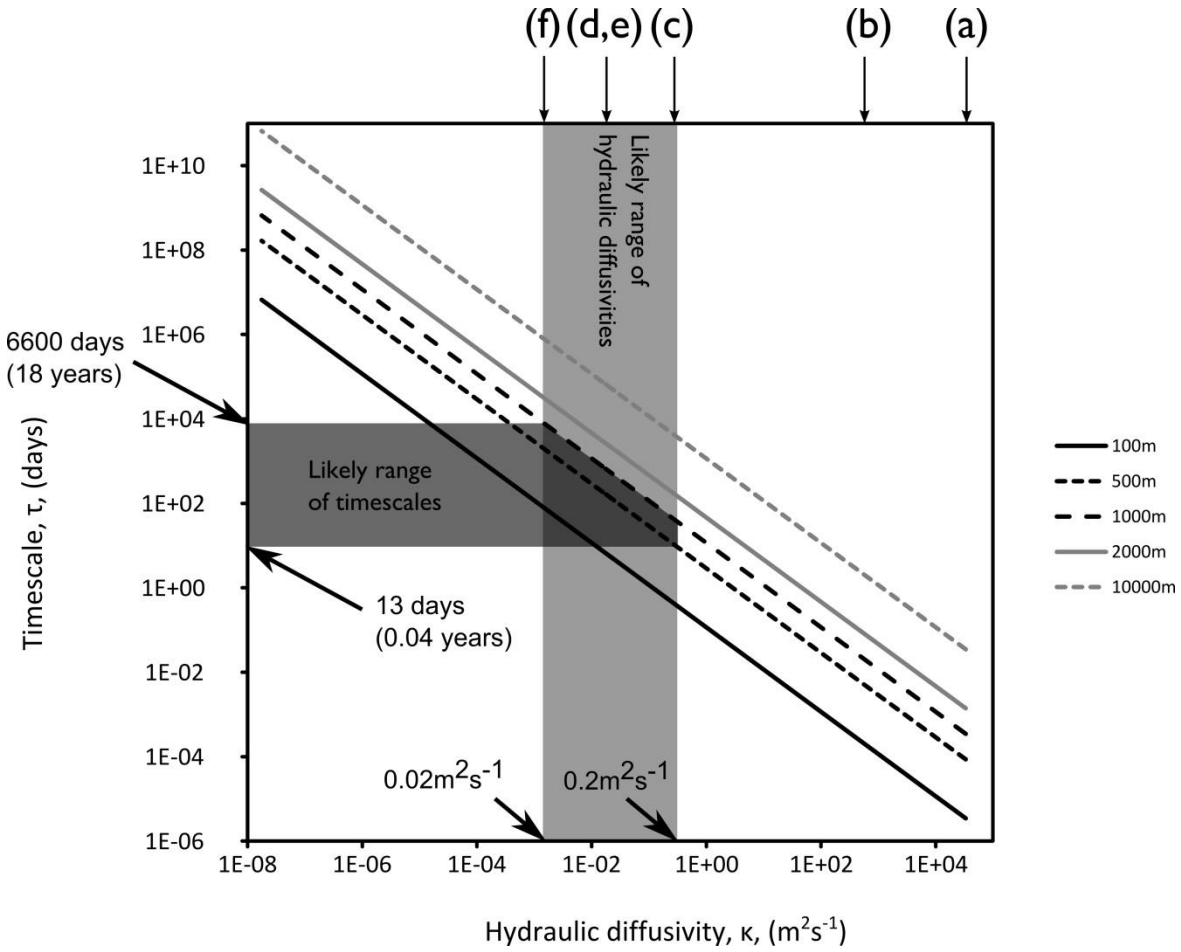
(f)
(d,e)
(c)
(b)
(a)
Likely range of hydraulic diffusivities
Likely range of timescales
6600 days (18 years)
13 days (0.04 years)
0.02m2s-1
0.2m2s-1
Timescale, τ, (days)
Hydraulic diffusivity, κ, (m2s-1)
1E+10
1E+08
1E+06
1E+04
1E+02
1E+00
1E-02
1E-04
1E-06
1E-08
1E-06
1E-04
1E-02
1E+00
1E+02
1E+04
100m
500m
1000m
2000m
10000m

Fig 12

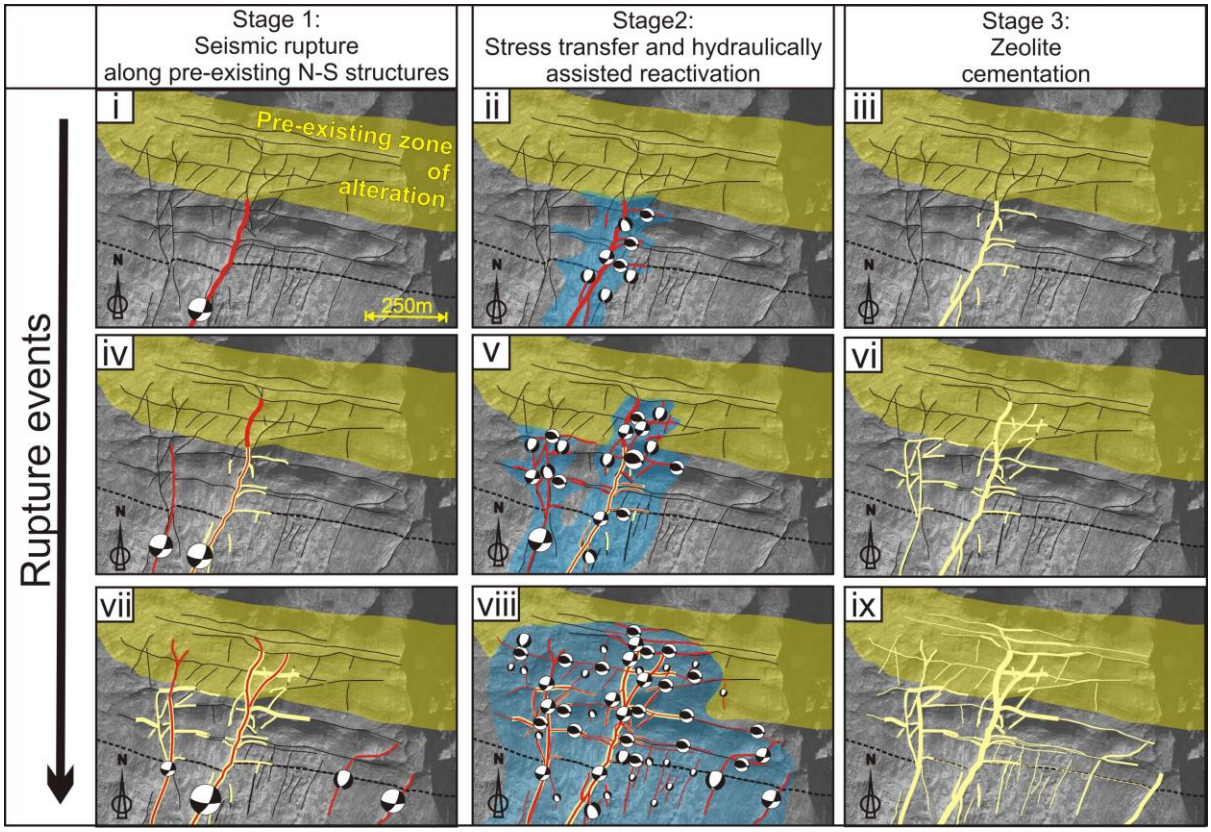
Stage 1:
Seismic rupture
along pre-existing N-S structures
Stage2:
Stress transfer and hydraulically
assisted reactivation
Stage 3:
Zeolite
cementation
Rupture events
i
ii
iii
iv
v
vi
vii
viii
ix
Pre-existing zone
of
alteration
250m
N

Fig 13

Fault type	**E-W rev**	**E-W rev**	**E-W rev**	**E-W rev**	**E-W rev**	**E-W rev**	**N-S nml**	**N-S nml**	**N-S Sin**	**N-S Sin**	**N-S Sin**	**N-S Sin**	**N-S Sin**	**N-S Sin**	**E-W rev**
Fault	T1	T1	T1	T1	T1	T1	S1 fracture zone	S1 fracture zone	S1 fracture zone	S1	S1	S1	S1	S2	T3
Sample	LFZ-1b	LFZ-1c1a	LFZ-1c1	LFZ-1c2	A03-07	A03-01	A03-04	A03-06	A03-05	LZF-20a	LZF-20b	LZF-20c	LZF20-d	LZF-13	LFZ-17b
% Laumontite	72	62	30	62	57	45	0	34	20	88	50	40	48	36	87
% Stiblite	0	0	0	0	0	55	58	44	55	0	0	0	0	0	0
% Stellerite	0	38	0	0	0	0	0	0	0	0	0	0	0	0	0
% Scolecite	0	0	0	0	0	0	42	22	16	0	0	0	0	0	0
% Prehnite	15	0	15	17	7	0	0	0	0	0	0	0	0	0	0
% Chlorite	8	0	9	13	7	5	0	0	0	0	0	0	0	7	3
% Quartz	5	0	10	8	29	0	0	0	9	0	0	0	6	27	10
% Albite	0	0	36	0	0	0	0	0	0	0	0	0	0	0	0
% K-Feldspar	0	0	0	0	0	0	0	0	0	12	50	60	46	31	0

Table 1

APPENDIX 1

Mineralogical analyses

X-Ray diffraction analysis (XRD) was performed at the Dipartimento di Geoscienze (Padua University) on powdered samples of the fault zone rocks (vein fills, gouges, cataclasites and ultracataclasites initially distinguished based on their colour in the field, e.g. Fig. 2b-c, 3e, 5a, 6c, 6d). All the samples were ground to a particle size <10 μm to minimize possible micro-absorption effects and to improve accuracy in measuring the intensities. X-ray powder diffraction data were recorded on a Panalytical θ-θ diffractometer (Cu radiation) equipped with a long fine focus Cu X-ray tube (operating at 40kV and 40mA), sample spinner, Ni filter and a solid state detector (X'Celerator). The system optics consist of fixed ½° divergent slit and 1° antiscatter slit on the incident beam path and soller slits (0.04 rad) on incident and diffracted beam path. The powders were mounted on 32 mm (internal diameter) circular sample holder. Scans were performed over the range 3-80° 2θ with a virtual step size of 0.017° 2θ and a counting time of 100 s/step. The phase identification and semi-quantitative analysis were performed using the software package X'Pert HighScore Plus. The phase identification was gained by the comparison with the reference pattern database Panalytical-ICSD (Inorganic Crystal Structure Database). The semi-quantitative data were calculated through the normalized RIR (Reference Intensity Ratio) method (Chung, 1974), using the scale factor measured and RIR values from ICSD database.

The XRD mineral abundances are reported in Table 1, but remain indicative and not necessary representative of the entire fault/fracture system. The error in weight % may range between ± 1% to ±5% depending on the number and type of minerals in the powder (e.g., phyllosilicates and clay minerals might be overestimated given their preferred orientation under the X-ray beam). The large scatter in the mineral abundance of individual samples

might also be due to the sampling technique: a representative analysis of the vein filling would have required a systematic sampling of each fault/fracture set, but this was not the goal of our study. The main minerals found (Table 1) were zeolites (the Ca-rich stilbite, scolecite and stellerite plus the Na- and Ca-rich laumontite), and prehnite plus quartz, albite, chlorite and K-feldspar (the latter four inside clasts of tonalite and sub-greenschist facies cataclasites: see for example Fig. 3a). The RIR semi-quantitative analysis showed variations in zeolite mineralogy and abundance depending on the type of fault (T, S and N, Fig. 1), fracture type (pure tensile or sheared) and host rock. For instance, if the occurrence of laumontite was widespread and independent of fault orientation (with the exception of sample A3-04 from S1), stilbite and scolecite were found only in the fillings of tensional fractures of the strike-slip (S) and normal faults (N). Conversely, samples taken from the thrust (T) group always included quartz (e.g., A03-07), whilst injection veins departing from the same T faults carry little or no quartz (sample A03-01). Multiple zeolite mineralization events (sample LFZ-1 in Fig. 6d) had almost the same zeolite mineralogy. The mineralogy of the zeolite-bearing veins also reflected the composition of the host-rocks. For instance, the zeolite-bearing faults exploiting aplite vein contacts were enriched in albite (sample LFZ-13 from fault T3) or those exploiting the sub- greenschist facies cataclasites were enriched in chlorite and quartz (sample A03-07 from T1).